Hindawi
Mathematical Problems in Engineering
Volume 2019, Article ID 4790250, 23 pages
https://doi.org/10.1155/2019/4790250

Research Article

Structural Strength Deterioration Characteristics and a Model of Undisturbed Loess under the Action of Wetting and Freeze-Thaw Cycles

Haicheng She,[1,2,3] **Zaiqiang Hu**,[1] **Zhan Qu**,[4] **Hongru Li**,[1] **Hu Guo**,[5,6] **and Xiaoli Ma**[3]

[1] *Institute of Geotechnical Engineering, Xi'an University of Technology, Xi'an 710048, China*
[2] *Key Laboratory of Failure Mechanism and Safety Control Techniques of Earth-rock Dam of the Ministry of Water Resource, Nanjing 210024, China*
[3] *YuLin Key Laboratory of Special Soil Mechanics and Engineering, Yulin University, Yulin 719000, China*
[4] *College of Petroleum Engineering, Xi'an Shiyou University, Xi'an, 710065, China*
[5] *School of Petroleum Engineering and Environment Engineering, Yan'an University, Yan'an 716000, China*
[6] *State Key Laboratory of Petroleum Resources and Prospecting, China University of Petroleum, Beijing 102249, China*

Correspondence should be addressed to Zaiqiang Hu; huzq@xaut.edu.cn and Hu Guo; truetutors@126.com

Received 5 September 2019; Accepted 22 November 2019; Published 30 December 2019

Academic Editor: Samuele De Bartolo

Undisturbed loess is affected by external environmental disturbances, such as wetting and freeze-thaw cycles, which cause microstructural changes that have an important impact on the structural strength of the loess. These changes in turn affect the stability of structures such as embankments, slopes, and guards. This article takes the Q_3 undisturbed loess in Lintong District, Xi'an, as an example. The effects of wetting and freeze-thaw cycles on the loess expansion ratio and pore structure were studied by wetting tests, freeze-thaw cycle tests, and scanning electron microscopy (SEM). The changes in the compression index and compression modulus were studied by a confined compression test. The loess e-lg$p$ compression curve was obtained according to the confined compression test, and the newly defined concepts of the loess structural strength, residual structural strength, and structural strength damage variable, in addition to the e-lg$p$ compression curve, were combined with the experimental data to calculate the damage value generated by the disturbance during the sampling and preparation of loess. The deterioration of the structural strength and damage variable of loess was analyzed. Based on the microscopic statistical damage theory and Weibull distribution, the model used the volume expansion ratio as a variable to establish a statistical damage model under wetting and freeze-thaw cycles. Finally, on the basis of the test, the model parameters were determined. The models were verified by taking loess from a foundation pit in the northern suburbs of Xi'an and were in good agreement with the results of the test. Ultimately, the models have good practicability and can provide guidance for engineering design and construction.

1. Introduction

Loess is a porous, weakly cemented Quaternary sediment and is mostly distributed [1, 2] in arid and semiarid regions in Asia, Europe, North America, and South America. Among all the countries in the world, China has the widest loess distribution area, the thickest and most complete strata, and the most complex genetic types and typical characteristics [3, 4]. As shown in Figure 1, China's loess is distributed mainly in Shanxi, Shaanxi, southeastern Gansu, and western Henan. In addition, there are sporadic distributions in Beijing, western Hebei, eastern Qinghai, Xinjiang, the Songliao Plain, Sichuan, Three Gorges, the Huaihe River Basin, and Nanjing. Loess forms a unique mineral composition with underconsolidated tiny structural units in a special sedimentary environment and complex and variable climatic conditions; consequently, loess has notable characteristics [5] such as a high water sensitivity, large pores, and low-pressure compaction, as shown in Figure 2.

The notable structural properties of loess [6] are the main reason why loess has unique physical and mechanical

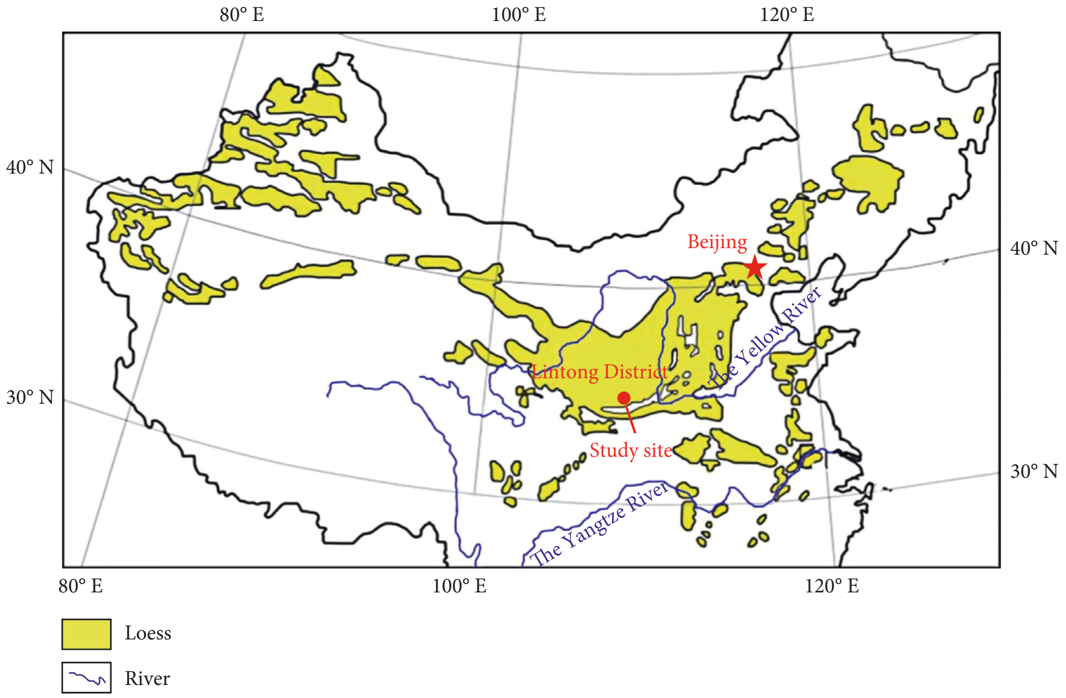

Figure 1: Distribution of loess in China.

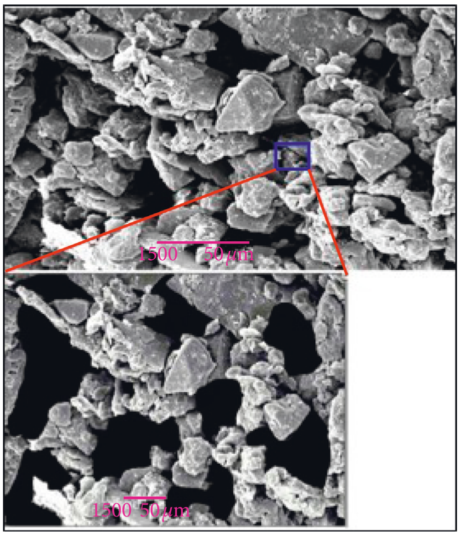

Figure 2: Loess microstructure.

properties, such as its collapsibility, compressibility, and shear strength; these structural properties are also the underlying cause of serious disasters in loess areas. Due to the differences among the geological features of loess areas, such as their geographical distribution, thickness variation, geological sequence, and material composition (particles, minerals and salts, etc.), the properties of loess are also regionally variable [7]. An in-depth understanding of the structural geological characteristics of regional loess is of great importance for solving the engineering geological problems in regional agriculture, industry, and urban construction. The core of geotechnical engineering research in loess regions is the analysis of the deformation, strength, and stability of loess in a complex external environment under mechanical disturbances. The most common loess disasters, as shown in Figure 3, primarily include loess landslides [8–11], collapses [12], loess collapsing [13, 14], ground collapse or subsidence [15, 16], ground fissures, and unstable slopes [17]. These disasters are of global concern because of their great cost to humans [8, 18–21]. The main factors inducing these loess disasters are natural causes such as earthquakes, rainfall, temperature changes, erosion of surface water, infiltration, and rivers as well as human activities such as excavation slopes, slope loading, blasting, reservoir water storage, and mining. Due to the disturbances of the external environment (such as the infiltration of underground and rainwater and temperature changes), the physical properties of loess microstructures, including their bonding and arrangement, are altered, and the structural strength deteriorates. The degree of deterioration of the loess structure, pore changes, and whether the soil structure is destroyed under external loading are closely related to wetting and freeze-thaw cycles and their interaction.

The structural strength of loess is a complex problem that has attracted extensive attention from scholars worldwide. As early as the early 20th century, people began to pay attention to the structure of the soil. A honeycomb structure [22], laminar structure [23], and disperse granular structure [24] have been proposed for soil; accordingly, the microstructure is important for evaluating soil strength and deformation. Soga [25] and Lafeber [26] presented the definition of soil structure based on Mitchell's understanding of the soil microstructure, namely, the geometric arrangement of soil particles, aggregates, and pores usually defined as the microscopic configuration of soil. Lohnes and Demirel [27] studied the strength and structure of laterites and lateritic soils. Gao [28] scanned


(a) (b) (c) (d) (e) (f)

Figure 3: Common types of loess disasters: (a) loess landslides; (b) collapses; (c) loess collapsing; (d) ground collapse; (e) ground fissures; (f) unstable slopes.

the microstructures of loess in various parts of northern China. Shen [29] asserted that the study of soil structure is the core of 21st century soil research. Xie and Qi [30] constructed a quantitative parameter reflecting structural properties based on compression deformation, also known as the comprehensive structural potential. Subsequently, Luo et al. [31] and Chen et al. [32] performed extensive work based on the idea of the comprehensive structural potential. Reznik [33] proposed a method for the calculation of soil structural pressure values. Liu et al. [34], Ahad [35], and Xu et al. [36] studied clay soil residual strength and shear strength characteristics.

To date, some studies have examined the influence of freeze-thaw cycles on the structural strength of loess. Edwin and Anthony [37] and Qi et al. [38] determined that the soil structure is affected by freeze-thaw cycles, which mainly change the microparticle cementation and arrangement of the soil and affect the changes in shear strength parameters. Johnson et al. [39] studied the effects of freeze-thaw cycles on the resilient properties of fine-grained soils. Similarly, Lu et al. [40] studied the effects of freeze-thaw cycles on the cracking of cohesive soils. Zhou et al. [41] and Xu et al. [42, 43] studied the effects of freeze-thaw cycles on mesostructural characteristics and mechanical behaviors using scanning electron microscopy (SEM) and soil mechanics tests.

Based on the above research, the present paper quantitatively studied the wetting and freeze-thaw cycles and the coupling of these two cycles. First, through laboratory experiments, the volume and structural pore variation of undisturbed loess samples and the deterioration of loess structural strength under the conditions of wetting and freeze-thaw cycles were studied. Second, the variables related to the structural strength were newly defined according to the undisturbed loess e-lg$p$ compression curve, and the basic equation of damage was established. Finally, based on microscopic damage mechanics theory and mathematical statistics, the statistical damage variables under wetting and freeze-thaw cycles and a statistical damage model of loess structural strength were constructed, the model parameters were determined, and the statistical damage model was verified.

2. Loess Deterioration Test

The soil samples were taken from the Q_3 loess of a foundation ditch in Lintong District, Xi’an. The soil has strong structural properties, and its buried depth is approximately 16 m. The essential properties and mineral composition of loess were analyzed by routine experiment and X-ray diffraction, as shown in Table 1.

The water-film transfer method (graded titration water injection method) was used to prepare loess samples with water contents of 9%, 15%, 20%, 25%, 30%, and saturated, and these samples were placed in a closed moisturizing tank for more than 3 days to ensure uniform water transport in the sample. The soil samples with the original water content and different water contents were subjected to 1, 2, 3, 6, 9, and 15 freeze-thaw cycles. Then, the confined lateral compression test was performed. Water migration loss occurred during the freeze-thaw cycles, and the test water was quantitatively supplemented according to the experimental statistical rules.

2.1. Test Schemes and Methods. The experiment simulated the changes in the volume and pore size of loess with an increase in the water content before and after the freeze-thaw cycles. The test schemes are shown in Table 2.

The samples were taken from free expansion deformation, in which the lateral direction is restricted, and to improve the measurement accuracy, the test measured the mass of the expanded portion. It can be seen from Table 1 that the loess samples represented expansive loess, and the amount of expansion was considered to depend upon water swelling and frost heaving. When undisturbed loess was used in the process of preparing samples with different water contents, a certain amount of expansion occurred in the sample during the wetting process, and a convex shape was formed on the upper and lower sides of the ring cutter. This convex part was considered to be caused by water swelling. With different water contents, after each freeze-thaw cycle, the loess sample also produced a certain amount of expansion, and a convex shape was formed on the upper and lower sides of the ring cutter. This convex part was considered to be caused by frost heaving. Specific research ideas and test procedures are shown in Figure 4.

2.1.1. Test Equipment. The main equipment used were as follows: ring cutter, ripper, plastic wrap, sealed bag, moisturizing jar, burette, electronic balance, freezer, and confined compression instrument.

2.1.2. Test Steps

(a) The prepared undisturbed loess samples were labeled according to the nomenclature in Table 2. The samples were moistened by the fractional titration water injection method, and 6 loess samples were prepared with water contents of 9%, 15%, 20%, 25%, 30%, and saturated.

(b) The prepared samples were wrapped with plastic wrap and placed in sealed bags and moisturizing jars and then allowed to stand for 72 hours to allow uniform water diffusion and sufficient water swelling. The convex parts from the upper and lower sides of the ring cutter were trimmed with a ripper, and the trimmed part of the loess was weighed and recorded as Δm_w.

(c) Loess samples 1-0, 2-0, 3-0, 4-0, 5-0, and 6-0 were subjected to a confined compression test (samples without freeze and thaw), and the remaining samples were placed in a freezer for 24 hours.

(d) After freezing for 24 hours, the samples with different water contents were observed for changes in volume; the convex parts from the upper and lower sides of the ring cutter were trimmed with a ripper, and the trimmed part of the loess was weighed and recorded as Δm_i, where i has a value of 1 for each freeze-thaw cycle.

(e) Loess samples 1-1, 2-1, 3-1, 4-1, 5-1, and 6-1 were subjected to a confined compression test, and the remaining samples were placed in a freezer for 24 hours.

(f) Test steps "d" and "e" were repeated, and finally, the cumulative frost heaving amount Δm_n after n freeze-thaw cycles was obtained, and the value was obtained by superposing Δm_i of each freeze-thaw cycle.

2.1.3. Test Considerations

(a) The test operation required a closed room with humidity of 40 to 60% and a temperature of 3°C to 6°C, but the temperature of the moisturizing jar was controlled at approximately 20°C

(b) In addition to trimming the expanded part, the plastic wrap and sealed bag were removed, but the remaining test samples needed to be resealed at any other time period

(c) If the amount of moisture lost from the samples by evaporation was too great, samples were replenished according to the constant mass of the test process

2.2. Volume and Pore Changing Test. The soil samples show axial free expansion deformation, which is confined laterally. To improve the measurement accuracy, the expansion ratio is calculated by measuring the mass of expansion, and the expansion is considered to be composed of water swelling and frost heave. Water swelling and frost heave change the microstructure, which in turn changes the density of loess. The expressions for density at different water contents (ρ_w) and density after each freeze-thaw cycle (ρ_n) are as follows:

$$\begin{aligned}\rho_w &= \alpha_w \rho,\\ \rho_n &= \alpha_n \rho,\end{aligned} \tag{1}$$

where ρ is the wet density of the original loess, g/cm^3, and α_w and α_n are density coefficients of change (test determination).

After each freeze-thaw cycle, the frost heave portion of the samples is trimmed. Then, the water swelling and each frost heave are cumulatively calculated. The free expansion rate (η) is calculated as follows:

Table 1: Essential parameters and mineral compositions of loess.

Essential parameters						Mineral compositions (%)				
d_s	w (%)	ρ (g/cm^3)	w_P (%)	w_L (%)	e_0	Quartz	Feldspar	Montmorillonite	Illite	Kaolinite
2.71	2.5	1.44	15.5	26.5	0.92	19.8	10.2	37.5	12.7	18.6

Table 2: Test schemes.

w (%)		2.5	9	15	20	25	30
Sample nomenclature	0 times	1-0	2-0	3-0	4-0	5-0	6-0
	1 time	1-1	2-1	3-1	4-1	5-1	6-1
	2 times	1-2	2-2	3-2	4-2	5-2	6-2
	3 times	1-3	2-3	3-3	4-3	5-3	6-3
	6 times	1-4	2-4	3-4	4-4	5-4	6-4
	9 times	1-5	2-5	3-5	4-5	5-5	6-5
	15 times	1-6	2-6	3-6	4-6	5-6	6-6

$$\Delta V_w = \frac{\Delta m_w}{\alpha_w \rho},$$

$$\Delta m_n = \sum_{i=1}^{n} \Delta m_i, \quad (2)$$

$$\Delta V_n = \frac{\Delta m_n}{\alpha_n \rho},$$

where ΔV_w is the expansion volume after water swelling, mm^3; ΔV_n is the cumulative volume after frost heave, mm^3; Δm_w is the expansion quality after water swelling, g; Δm_n is the cumulative mass after frost heave, g; and Δm_i is the mass increase of frost heave per freeze-thaw cycle, g.

After the volume variable in the calculation formula of the expansion ratio is changed to the mass variable, the water swelling rate (η_w) and the frost heave rate (η_n) can be expressed as follows:

$$\eta_w = \frac{\Delta m_w}{\alpha_w m} \times 100\%,$$

$$\eta_n = \frac{\Delta m_n}{\alpha_n m} \times 100\% = \frac{\sum_{i=1}^{n} \Delta m_i}{\alpha_n m} \times 100\%, \quad (3)$$

$$\eta = \eta_w + \eta_n,$$

where η_w is the water swelling rate, η_n is the frost heave rate, η is the free expansion rate, and m is the ring cutter mass, g.

The calculation formula for calculating the void ratio of the soil sample according to the volume expansion ratio is as follows:

$$e_w = e_0 + (1 + e_0) \cdot \eta_w, \quad (4)$$

$$e_n = e_w + (1 + e_w) \cdot \eta_n, \quad (5)$$

where e_w is the void ratio after water swelling and e_n is the void ratio after frost heave.

According to the experimental measurements of the pore ratio and volume change of samples and the use of equations (4) and (5) to calculate the volume and pore change of the loess after water swelling and frost heave, the results are as shown in Figures 5–7.

Figures 5–7 show the following. (1) As the water content increases, the initial volume changes slowly, and after the water content exceeds 16%, the volume change rate increases significantly, indicating that the loess is an expansive loess. (2) The volume change rate is faster during the first 3 freeze-thaw cycles and then slows down. After 9 cycles, the change is gradual, indicating that the loess structure is broken at the initial stage of the freeze-thaw cycles, and a new structure is formed, and as the number of freeze-thaw cycles increases, the new structure will tend to be stable. (3) Due to the correlation between the void ratio and the expansion ratio, the variation in the void ratio with the water content and the freeze-thaw cycles is consistent with the change in the expansion ratio.

In short, the volume expansion of loess samples with wetting and freeze-thaw cycles is worthy of our attention; the reasons for these changes can be summarized as follows. (1) When the water content of the loess sample is low, the volume expansion produced is small. On the one hand, the reason is that the matrix suction of loess makes the water difficult to diffuse or spread unevenly, the local structural strength in the sample is weakened, and the overall structural strength is disturbed a little. On the other hand, due to the insufficient hydration of the loess sample, it produces a small hydration expansion force, which is difficult to overcome the structural strength of the loess. When the water content of the loess sample is high, the volume expansion ratio of the sample is significantly accelerated. The reason is that the water diffusion and hydration of the loess sample can be fully achieved. (2) In the previous freeze-thaw cycles, the rate of frost heave increases rapidly, and as the water content increases, the growth rate is more significant. The reason is that the water inside the loess sample is frost heave, which changes the internal structure of the loess and also increases voids and pores that contain moisture. After freeze-thaw cycles reach a certain value, the rate of frost heave becomes slower. The reason is that the loess sample is not subjected to any load and there is no thawing collapse after frost heaving; that is, the loess structure change is basically not recovered. The expansion volume is mainly caused by local frost heaving after moisture migration, so the expansion rate is slowed down.

2.3. Loess Microstructural Test. A JSM-6700F scanning electron microscope (SEM) was a field emission scanning electron microscope made in Japan, which was mainly composed of an electro-optical system, a scanning system, a signal detection amplification system, an image display and recording system, a power supply, and a vacuum system (see Figure 8). The SEM was used to scan the undisturbed

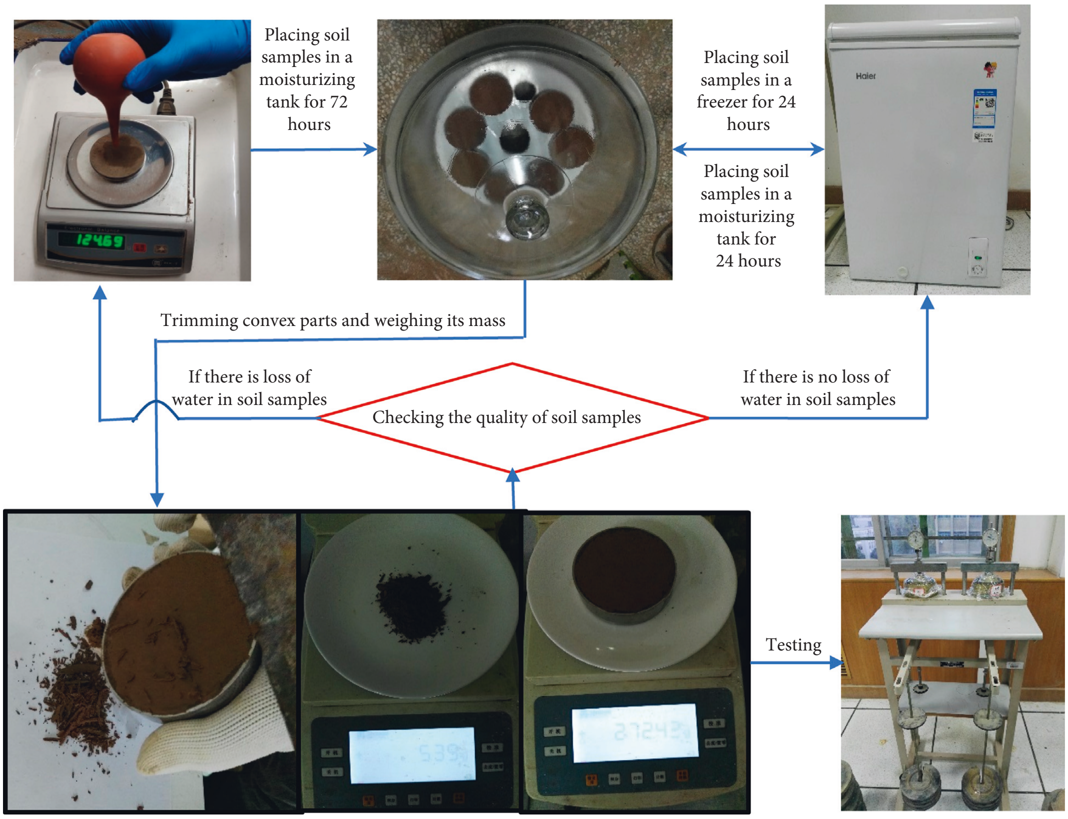

Figure 4: Research ideas and test procedures.

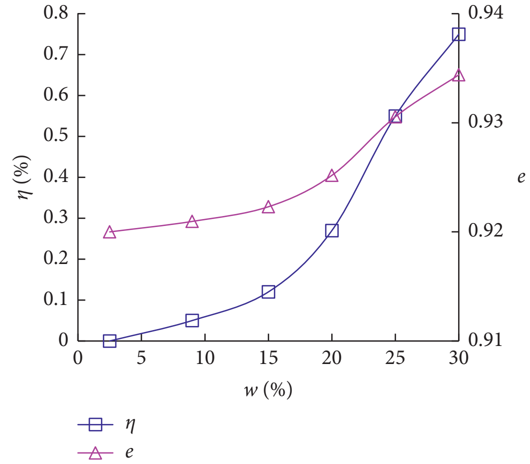

Figure 5: Volume change and void ratio after wetting.

sample, the sample with a water content of 20%, and samples exposed to 1, 2, 6, and 9 freeze-thaw cycles with a water content of 20%. The changes in the microscopic pore structure were studied.

2.3.1. SEM Image Processing and Analysis. The SEM images were processed by MATLAB for grayscale adjustment, enhancement, iterative denoising, etc., and the binarization images were obtained as shown in Figure 9.

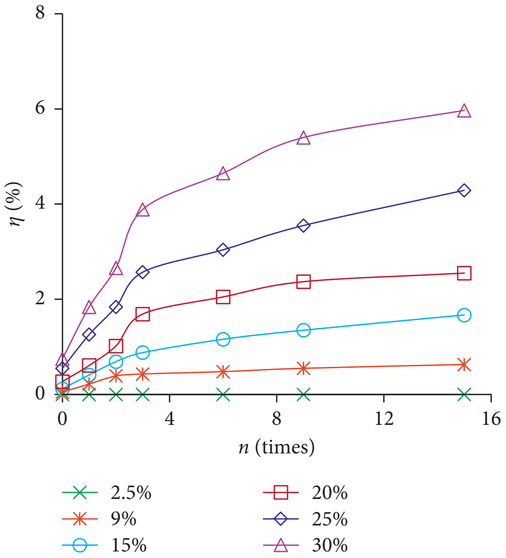

Figure 6: Volume change after freeze and thaw cycles.

A large number of fine pores and fewer large pores are found in the undisturbed loess, and its microstructure exhibits a dense overall structure (Figure 9(a)). During the wetting process, the rapid flow of water along the large pores will increase the throat diameter of the original pores. Then, the water infiltrates into the surrounding fine pores along the large pore wall, and large granules and clots appear due to the wetting expansion and suction (Figure 9(b)). As the

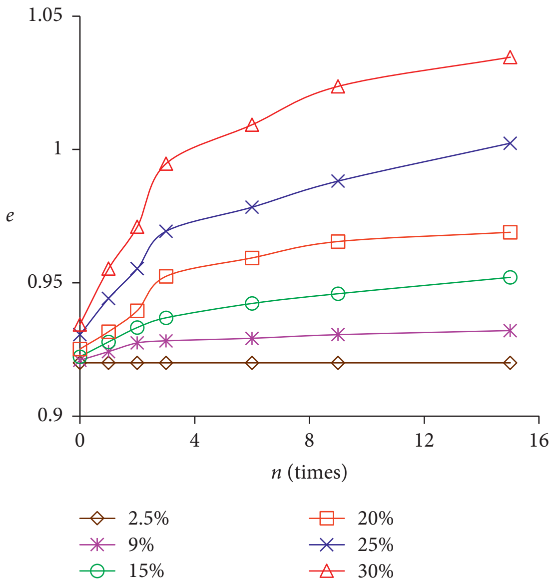

Figure 7: Void ratio change after freeze and thaw cycles.

Figure 8: A JSM-6700F scanning electron microscope (SEM).

number of freeze-thaw cycles increases, the fine pores decrease, the large pores increase significantly, the maximum pore throat diameter can reach 35 μm, and the shape and distribution of the pore structure also change (see Figures 9(c)–9(f)).

The microstructure quantitative analysis of all the images in Figure 9 employs the image analysis software Image-Pro Plus 6.0 (IPP 6.0), which is widely used in medical, biological, industrial, and other fields. IPP 6.0 is image processing software that can capture the area, diameter, angle, perimeter, and roundness of the image. A calibration space scale is first applied on an image of a certain magnification to establish a unit of measurement associated with the image. The spatial measurement scale associated with the magnified image is constructed later. In general, IPP 6.0 will measure all the space in pixels; therefore, the spatial scale is changed so that IPP performs the measurement in microns. The specific processing steps are as follows. (a) The pixel ratio is set because the actual image is calculated in pixels, and the spatial scale is defined by the length; therefore, the length needs to be defined according to the scale of the SEM image (Figures 10 and 11). (b) The unknown parameters are selected and calculated. The parameters of the microstructure of the loess are mainly the void ratio and the particle size (Figure 12). (c) According to statistical analysis of the target parameters of the image, the statistical results of particle size and void change with wetting and freeze-thaw cycles are obtained, and the microstructural changes of the loess are quantitatively analyzed.

Each selected microarea was analyzed using PPI software as shown in Figure 13, and the maximum and minimum pore and particle size were obtained. The average value of the maximum value and the minimum value is taken as the parameter value of the minute area. Finally, the values of each regional parameter are cumulatively calculated, and the results of quantitative analysis of pores and particles are obtained as follows.

2.3.2. Quantitative Analysis of Particles.

The statistical results were used to analyze the variation in the average particle size of the loess particles with the undisturbed loess and 20% water content loess following 0, 1, 3, 6, and 9 freeze-thaw cycles.

Figure 14 shows that particle sizes ($d < 2\,\mu$m) gradually decreased with the freeze-thaw cycles, and particles ($2 < d < 5\,\mu$m, $5 < d < 20\,\mu$m, and $d > 20\,\mu$m) increased in fluctuation, indicating that freeze-thaw cycles reduce cohesiveness and increase both particle size and agglomeration.

2.3.3. Quantitative Analysis of Pore Size.

According to the average pore size, the pores in the soil were divided into extra-large pores ($r > 50\,\mu$m), large pores ($20 < r < 50\,\mu$m), medium pores ($5 < r < 20\,\mu$m), small pores ($2 < r < 5\,\mu$m), and micropores ($r < 2\,\mu$m). The statistical results were used to analyze the variation in the pore diameter of loess with the undisturbed loess and 20% water content loess following 0, 1, 3, 6, and 9 freeze-thaw cycles.

Figure 15 shows that the loess sample pores were mainly mesopores, small pores, and micropores, with relatively few extra-large pores and large pores. Microporosity decreased with the distribution of freeze-thaw cycles. The sizes of small pores and small and medium pores increased with the number of freeze-thaw cycles. The sizes of extra-large pores and large pores increased slightly.

The areas occupied by the pores or soil particles in the cross-sectional area were calculated using IPP 6.0. The plane porosity ratio can be approximated as follows at a 20% water content or after different freeze-thaw cycles:

$$\begin{aligned} e_w &= \frac{S_{aw}}{S_{sw}} \times 100\%, \\ e_n &= \frac{S_{an}}{S_{sn}} \times 100\%, \end{aligned} \tag{6}$$

where e_w is the porosity ratio at different water contents; e_n is the porosity ratio after different freeze-thaw cycles; S_{aw} and S_{an} are the areas occupied by the pores at different water contents or after different numbers of freeze-thaw cycles, respectively; and S_{sw} and S_{sn} are the

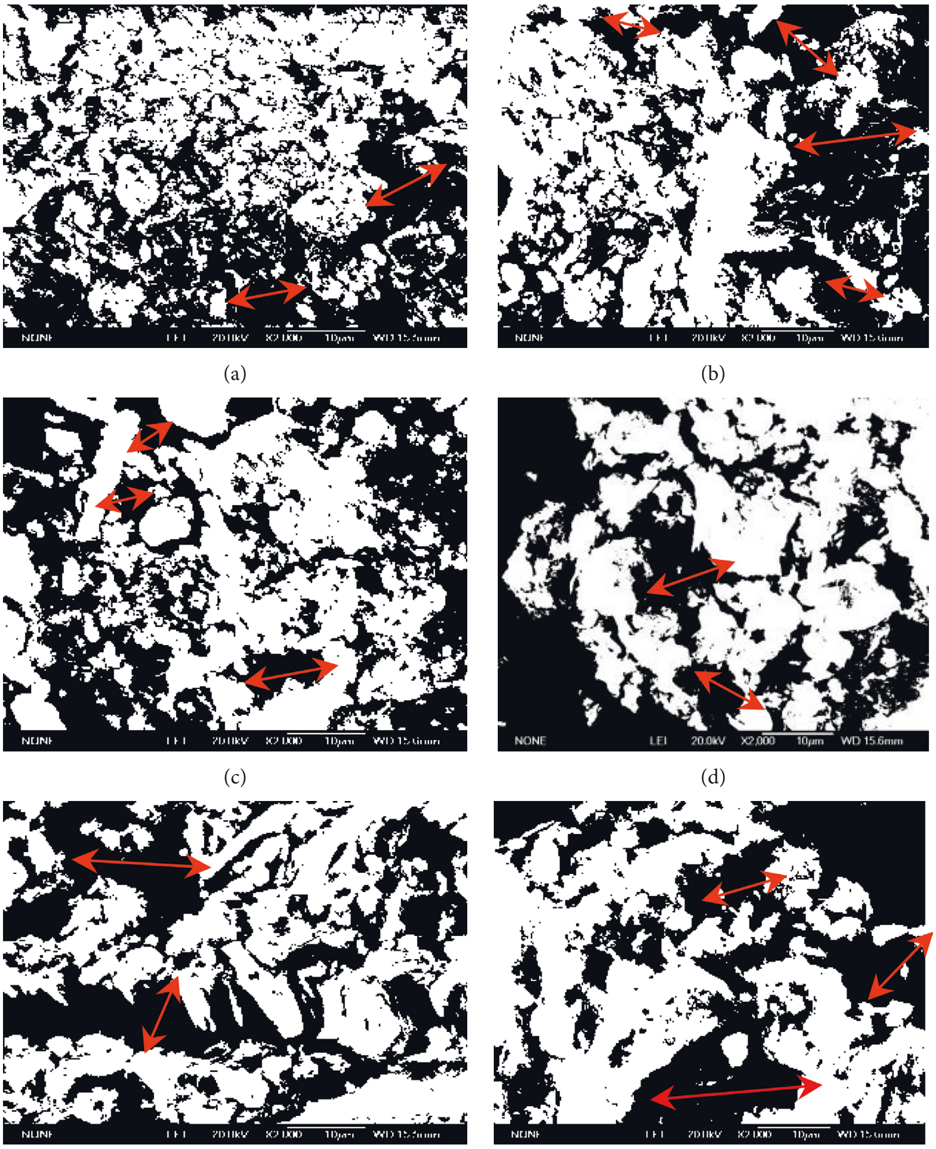

(a) (b)

(c) (d)

(e) (f)

Figure 9: Binarization images of SEM: (a) undisturbed loess samples; (b) $w = 20\%$; (c) $w = 20\%$ and $n = 1$ time; (d) $w = 20\%$ and $n = 3$ times; (e) $w = 20\%$ and $n = 6$ times; (f) $w = 20\%$ and $n = 9$ times.

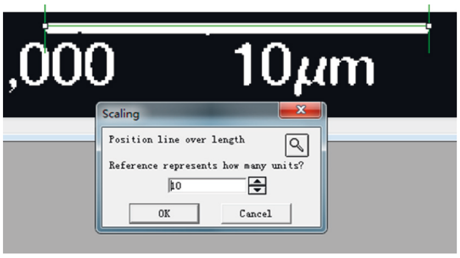

Position line over length

Reference represents how many units? 10

Figure 10: Pixel scale setting.

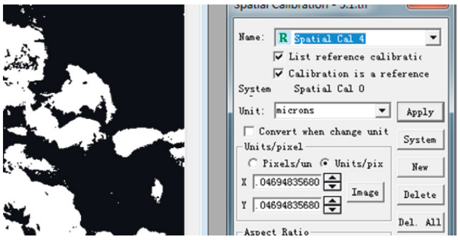

Name: R Spatial Cal 4

☑ List reference calibratic

☑ Calibration is a reference

System Spatial Cal 0

Unit: microns

☐ Convert when change unit

Units/pixel

○ Pixels/un ● Units/pix

X .04694835680

Y .04694835680

Figure 11: Pixel and micron conversion. (a) Particle selection. (b) Pore selection.

areas occupied by soil particles at different water contents or after different numbers of freeze-thaw cycles, respectively.

The expansion ratios η_w and η_n at different water contents or after different numbers of freeze-thaw cycles can be obtained by equations (4) and (5):

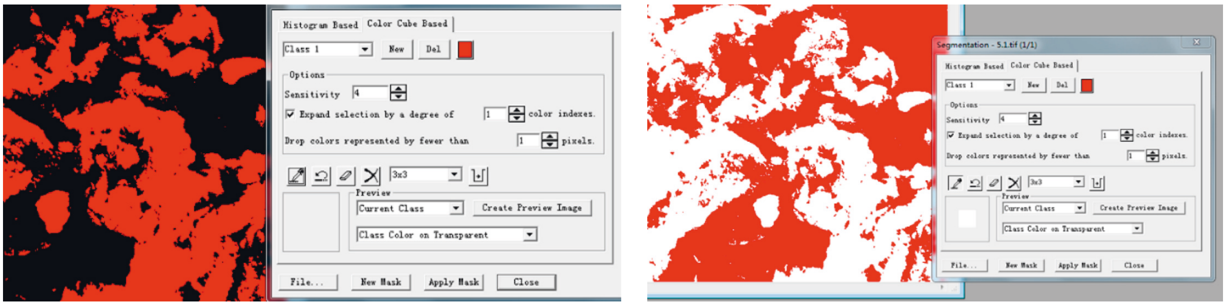

Class 1

Sensitivity 4

☑ Expand selection by a degree of 1 color indexes.

Drop colors represented by fewer than 1 pixels.

3x3

Current Class

Class Color on Transparent

Segmentation - 5.1.tif (1/1)

Class 1

Sensitivity 4

☑ Expand selection by a degree of 1 color indexes.

Drop colors represented by fewer than 1 pixels.

3x3

Current Class

Class Color on Transparent

(a) (b)

Figure 12: Target selection. (a) Pore size. (b) Particle size.

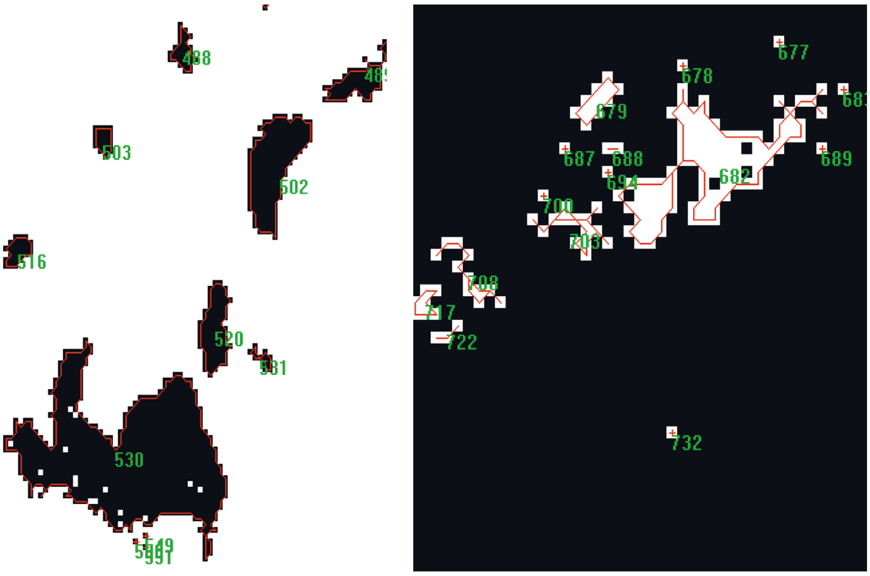

(a) (b)

Figure 13: Target calculation.

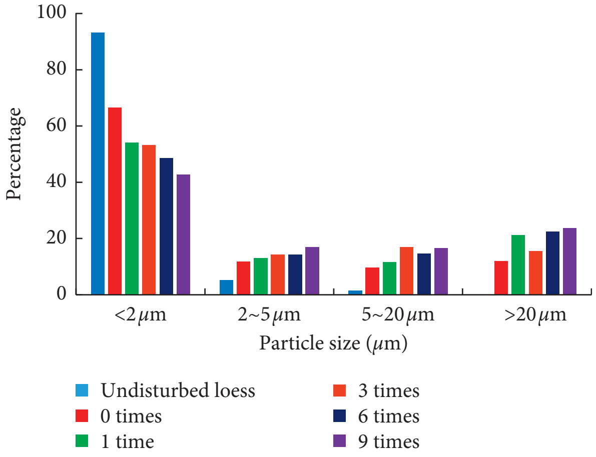

Figure 14: Particle size changes with freeze-thaw cycles.

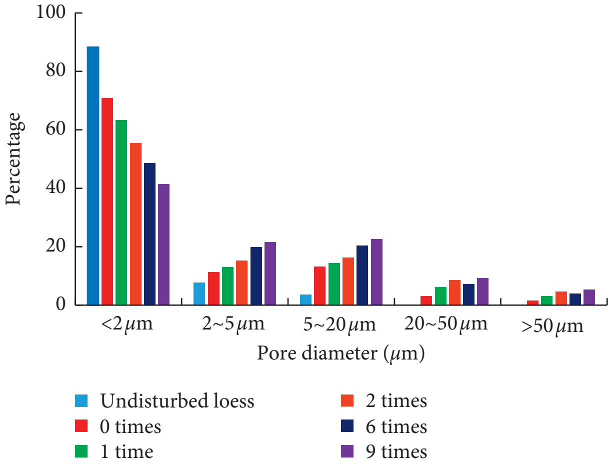

Figure 15: Pore size changes with freeze-thaw cycles.

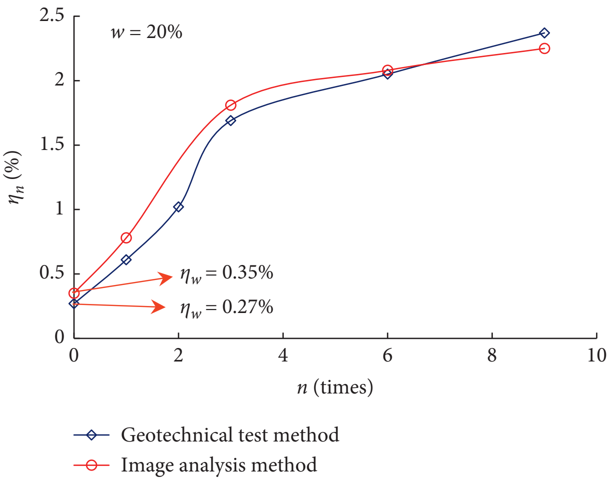

FIGURE 16: Comparison of geotechnical test and digital image analysis methods.

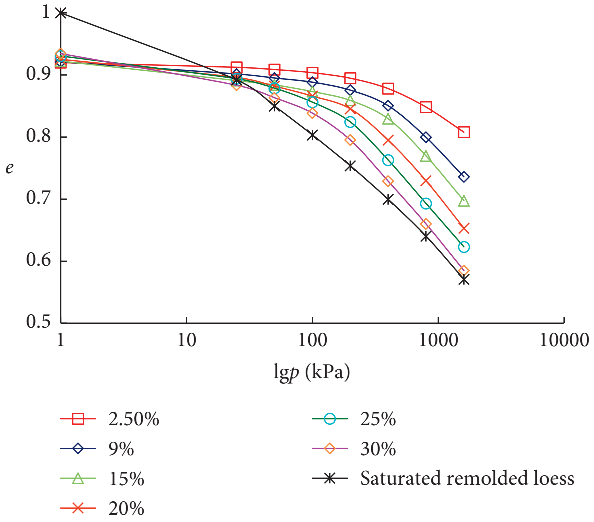

FIGURE 17: *e*-lg*p* curve with increasing water content: (a) $w = 2.5\%$; (b) $w = 9\%$; (c) $w = 15\%$; (d) $w = 20\%$; (e) $w = 25\%$; (f) $w = 30\%$.

$$\eta_w = \frac{e_w - e_0}{1 + e_0},$$
$$\eta_n = \frac{e_n - e_w}{1 + e_w}. \tag{7}$$

By comparing the geotechnical test method and the digital analysis method of loess microstructure images, the conclusions are as follows.

Figure 16 shows that the loess expansion rate determined according to the digital image analysis method is slightly higher than the loess expansion rate determined by the geotechnical test method, but as the number of freeze-thaw cycles increases, the results of the two methods exhibit the opposite trend, although the difference is small. Therefore, the use of digital image analysis has unique advantages in studying the pore structure and variation of undisturbed loess.

2.4. Confined Compression Test. The strength test was applied to different samples after the simulated wetting and freeze-thaw cycles. The void ratio of the samples was not the initial void ratio; instead, the void ratio after the freeze-thaw cycles was used as the void ratio for each test. In this paper, the confined compression test was used to measure the deterioration of the structural strength of the loess, as shown in Figures 16 and 17.

(1) Figure 17 shows that as the water content increases, the compression index C_c increases and the compression modulus E_s decreases, which indicates that the cementation strength and the friction strength between the soil microstructures of the loess decrease with the increase in the water content, reducing the strength of the loess structure. (2) Figures 18(a) and 18(b) show that when $w \leq w_P$, the compression index C_c and the compression modulus E_s change little as the number of freeze-thaw cycles increases, which indicates that the volume increase due to the water phase change has little effect on the structural strength of the loess. (3) Figures 18(c)–18(f) show that when $w_P < w \leq w_L$, the compression index C_c increases greatly with the number of freeze-thaw cycles, and the compression modulus E_s changes less, which indicates that the volume increase due to the water phase change has a greater influence on the spatial arrangement of the microstructure, and thus, the structural strength is reduced at a faster rate. When $w > w_L$, the compression index C_c and the compression modulus E_s both change slowly with the number of freeze-thaw cycles, which indicates that the loess has rheological properties and that the microstructure of the loess is self-healing due to the rheological action after the solid water melts; thus, the rate of structural strength reduction is slowed down.

3. Deterioration of the Loess Structural Strength

Loess structural properties include the composition, shape and arrangement of the skeleton particles, internal pore characteristics, types of cementing material, and degree of cementation. Under external environmental disturbances such as wetting and freeze-thaw cycles, the volume of loess changes, which causes the particle distribution and pore structure to change. Soil and water action can reduce the bonding force of the cementing material between the loess microparticles or the microparticle aggregates, and the lubricating property of water significantly reduces the friction between the microparticles or the microparticle aggregates, reducing the structural strength of the loess. Because water in the micropores produces uneven migration and distribution and phase change occurs during the freeze and thaw process, the volume of water is changed; then, the soil samples produce frost heave, which causes the loess internal structure to be further damaged.

3.1. Loess Structural Strength and Damage Variables. Loess structural strength is a kind of cementing strength formed during the formation of the soil structure. Structural strength is generated with the formation of soil structure and disappears with the destruction of soil structure. Its value is

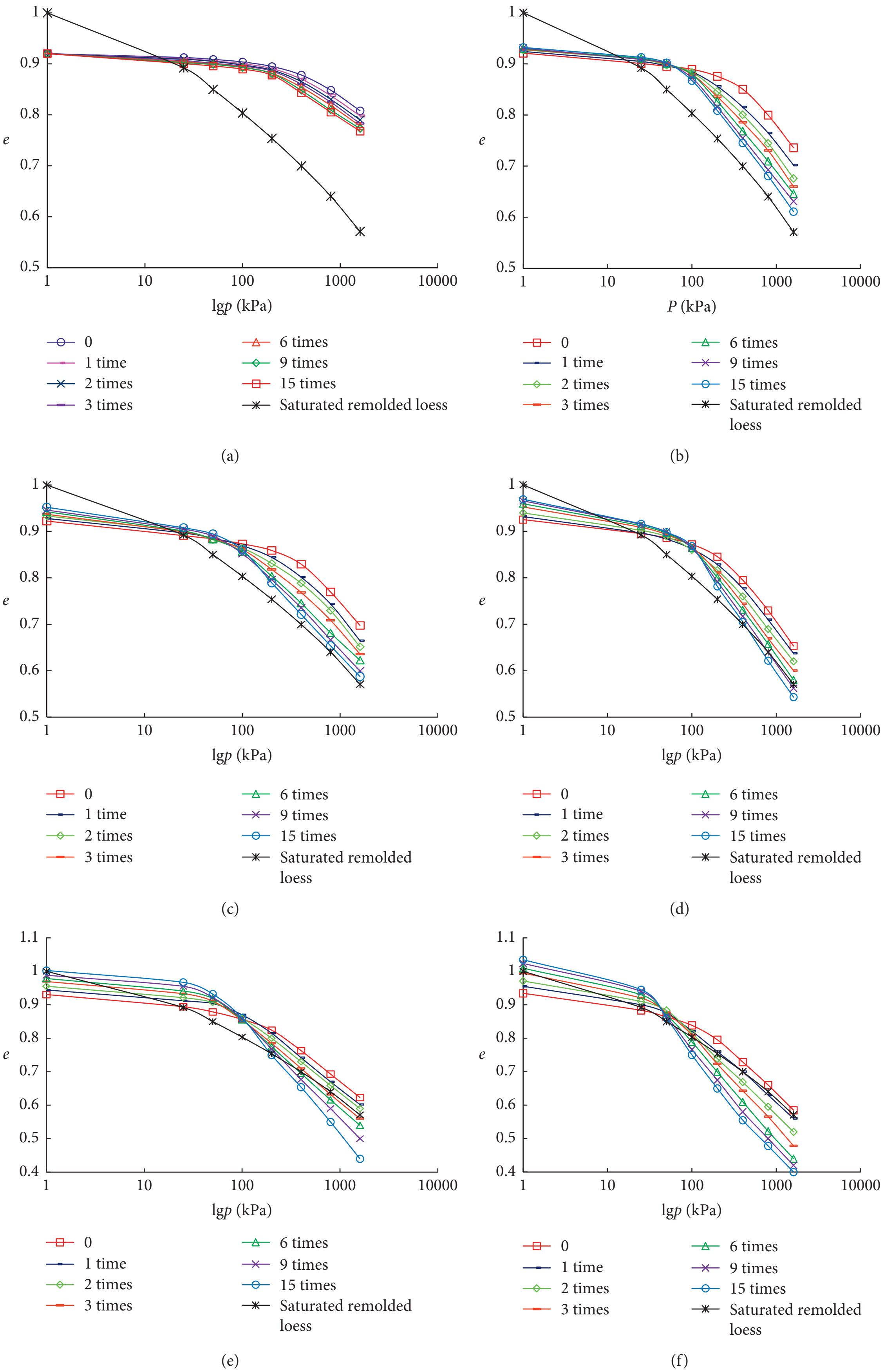

(a) (b) (c) (d) (e) (f)

FIGURE 18: e-lg$p$ curve with increasing number of freeze-thaw cycles: (a) $w = 2.5\%$; (b) $w = 9\%$; (c) $w = 15\%$; (d) $w = 20\%$; (e) $w = 25\%$; (f) $w = 30\%$.

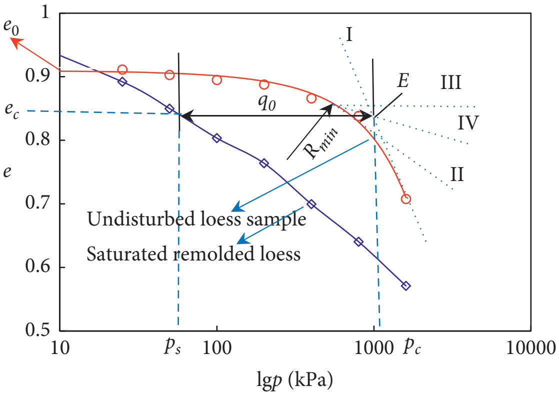

Figure 19: Structural strength of undisturbed loess (note: I is the straight line fitting the end of the compression curve, II is the tangent of the point of maximum curvature, III is the horizontal straight line passing the maximum curvature point, and IV is the angle bisector of straight lines II and III.).

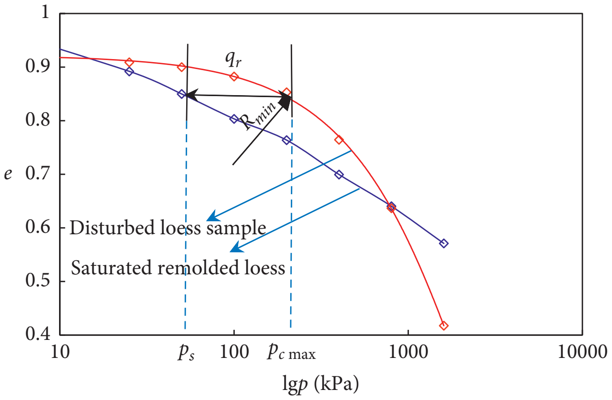

Figure 20: Residual structural strength of loess.

determined by the cementing force and friction between the microparticles or the microparticle aggregates.

The cementing force is a short-range force, including the chemical bonding force, molecular gravity, and suction between the microparticles or the microparticle aggregates, which form the cementing structural strength of loess. Friction is a long-range force, including the friction and interlock force between soil particles or the particle aggregates that form the friction structural strength of loess. Friction is the force that prevents the deformation of loess when the connecting force between the microparticles or the microparticle aggregates is overcome by mutual dislocation, displacement, and rearrangement movements.

Dang and Li [44] analyzed the unsaturated loess composition to determine the strength and sources of structural strength, developed a method for determining the structural strength, and studied its variation. Hu et al. [45] used the confinement compression test to determine undisturbed loess structural strength and studied its variation. Tian et al. [46, 47] quantitatively described the loess structural parameters, that is, the variation in the cementing structural strength and friction structural strength of loess. Yin et al. [48] analyzed transport of liquid water, vapor, stress, and heat in unsaturated freezing soil. Lu et al. [40, 49] and Tang et al. [50] analyzed cracking characteristics and established constitutive relations and mechanical degradation of expansive soil under freeze-thaw cycles. Liu et al. [51] researched mechanical behavior and the constitutive model of tailing soils subjected to freeze-thaw cycles. Liu et al. [52] established an elastoplastic model for saturated freezing soils based on thermo-poromechanics. Zhang et al. [53] used a new novel constitutive model to simulate the rock failure under freeze-thaw cycles.

The present authors believe that the e-lg$p$ compression curve can be analyzed from the flat linear phase of the elastic deformation to the local microstructure damage, and the curvature of the line segment suddenly increases in plastic deformation. The pressure corresponding to the maximum point of curvature is defined as the disturbance to the original structural strength of the original loess caused by the sampling process. To investigate the influences of sampling and the process of preparing samples on the structural strength of undisturbed loess, the pressure difference between the point corresponding to the preconsolidation pressure and the pore ratio at the point corresponding to the saturated remolded loess indicates that the structural strength of the undisturbed loess is greater reasonable. The structural strength q_0 of the undisturbed loess is shown in Figure 19.

The structural strength of the undisturbed loess can be expressed as follows (see Figure 19):

$$q_0 = p_c - p_s. \tag{8}$$

The preconsolidation pressure is most often determined by the Casagrande [24] drawing method, which requires strict testing operations and data reading to ensure accuracy.

For the structural strength of the loess affected by the external environment (wetting, temperature change, loading, etc.), the e-lg$p$ compression curve has a significant turning point, which is also considered to be the starting point of the failure of the loess microstructure and the corresponding void ratio. The external environment disturbs the maximum pressure difference between the original loess and the saturated remolded loess. This value is defined as the residual structural strength q_r of loess, as shown in Figure 20.

$$q_r = p_{c\,\max} - p_s. \tag{9}$$

Based on the principle of damage mechanics, the damage variable is defined as follows:

$$D = \frac{q_0 - q_r}{q_0} = 1 - \frac{q_r}{q_0}. \tag{10}$$

In general, D is between 0 and 1. When $D = 0$, it indicates that there is no disturbance damage, that is, the state of the original stratum. When $D = 1$, it indicates that the state of the original stratum is fully disturbed, that is, the state of saturation remolding.

q_{0r} replaces q_r to indicate the residual structural strength of undisturbed loess after sampling and preparation of samples; then, equation (10) changes to the following:

$$D_d = \frac{q_0 - q_{0r}}{q_0} = 1 - \frac{q_{0r}}{q_0}, \tag{11}$$

where D_d is the sampling and sample preparation disturbance damage variable. Its numerical size reflects the different degrees of disturbance caused by the release of pressure on the formation and sampling and preparation of samples after excavation. The higher the value, the larger the disturbance.

D_d can be obtained according to the e-lg$p$ compression curve. First, the pressure values at the turning point of the fitting curve (the maximum curvature point) and the preconsolidation pressure are determined.

3.2. Pressure at the Turning Point.

According to the test curve (Figure 19), a univariate function model with a higher order is satisfied. Since the abscissa is a function, let $x = \lg(p/\mathrm{Pa})$; then, set the function as follows:

$$e(x) = a_1 + a_2 x + a_3 x_2 + \ldots + a_n x^{n-1} + a_{n+1} x^n, \tag{12}$$

where n is a natural number. Its size depends on the shape of the curve. The general value is 3-5, and the value of the saturated remolded loess is 1. a_i is the coefficient of fitting the mathematical expression, $i = 1, 2, 3, \ldots, n$.

For convenience of discussion, take $n = 3$ and substitute $e(x)$ into the curvature calculation formula to obtain the curvature value of the curve:

$$K = \frac{\left|e''(x)\right|}{\left[1 + \left(e'(x)\right)^2\right]^{3/2}} = \frac{\left|2a_3 + 6a_4 x\right|}{\left(1 + \left(a_2 + 2a_3 x + 3a_4 x^2\right)^2\right)^{3/2}}. \tag{13}$$

To perform the maximum curvature method, the absolute elimination in equation (13) is changed to the function extremum problem, all the maxima and the limit values are compared to the absolute value, and the maximum value is the maximum curvature of the test curve. The point corresponding to the maximum curvature is the turning point and the point of maximum curvature. The point corresponding to the void ratio and pressure is the starting point of the failure of the loess microstructure. Therefore, let

$$\left[\frac{2a_3 + 6a_4 x}{\left(1 + \left(a_2 + 2a_3 x + 3a_4 x^2\right)^2\right)^{3/2}}\right]' = 0. \tag{14}$$

Equation (14) can be simplified to obtain a one-dimensional quadratic equation:

$$Ax^4 + Bx^3 + Cx^2 + Dx + E = 0, \tag{15}$$

where $A = 90a_4^3$, $B = 120a_3a_4^2$, $C = 52a_3^2a_4 + 24a_2a_4^2$, $D = 16a_2a_3a_4 + 8a_3^3$, and $E = 4a_2a_3^2 - 2a_2^2a_4 - 2a_4$.

A solution to the equation according to the Ferrari method can be obtained as follows:

$$x_n = \frac{-B + (-1)^{n/2} m + (-1)^{n+1}\sqrt{S + (-1)^{n/2} T}}{4A}, \quad n = 1, 2, 3, 4, \tag{16}$$

where

$$\begin{aligned}
m &= \sqrt{B^2 - \frac{8}{3}AC + 4A\left(\omega^{k-1}u + \omega^{4-k}v\right)}, \quad k = 1, 2, 3, \\
S &= 2B^2 - \frac{16}{3}AC - 4A\left(\omega^{k-1}u + \omega^{4-k}v\right), \quad k = 1, 2, 3, \\
T &= \frac{8ABC - 16A^2D - 2B^3}{m}, \\
u &= \sqrt[3]{Q \pm Z} \text{ (take the larger value of norm)}, \\
v &= \frac{P}{u} \text{ (if } u \text{ is zero, then } v \text{ also has a value of zero)}, \\
\omega &= -\frac{1}{2} + \frac{\sqrt{3}}{2}i, \\
P &= \frac{C^2 + 12AE - 3BD}{9}, \\
Q &= \frac{27AD^2 + 2C^3 + 27B^2E - 72ABC - 9BCD}{54}, \\
Z &= \sqrt{Q^2 - P^2}.
\end{aligned} \tag{17}$$

Considering the boundary conditions, the invalid solution of equation (16) is omitted, and the point $R_{\min}$ $(\lg p_{c\max}, e_{c\max})$ at which the maximum value of K is obtained is the maximum curvature point, that is, the minimum radius of curvature at this point. Then,

$$\lg p_{c\max} = \frac{-B + (-1)^{n/2} m + (-1)^{n+1}\sqrt{S + (-1)^{n/2} T}}{4A}, \quad n = 1, 2, 3, 4. \tag{18}$$

When n equals 1 or 3, the result is an irrational number, which is an invalid solution. When n equals 2 or 4, the results are opposite to each other and take a positive value.

3.3. Preconsolidation Pressure.

The preconsolidation pressure is determined by the Casagrande method. First, the line equations of I, II, and IV (Figure 19) need to be determined separately.

The line I equation is obtained by linear regression analysis, and the test data $(e_i, \lg p_i)$, $i = 1, 2, 3, \ldots, m$ are taken at the end of the compression curve.

Then, the linear regression equation is set to

$$e = \widehat{\beta}_0 + \widehat{k}_1 \lg p, \tag{19}$$

where $\widehat{\beta}_0$ and $\widehat{k}_1$ are estimated values of β_0 and k_1, respectively, and $\widehat{\beta}_0$ and $\widehat{k}_1$ must be estimated using the least squares method.

$$\begin{aligned}
\widehat{\beta}_0 &= \overline{e} - \widehat{k}_1 \overline{\lg p}, \\
\widehat{k}_1 &= \frac{\sum_{i=1}^{m}\left(\lg p_i - \overline{\lg p}\right)\left(e_i - \overline{e}\right)}{\sum_{i=1}^{m}\left(\lg p_i - \overline{\lg p}\right)^2},
\end{aligned} \tag{20}$$

where $\overline{\lg p} = (1/m)\sum_{i=1}^{m} \lg p_i$ and $\overline{e} = (1/m)\sum_{i=1}^{m} e_i$.

The line II equation is expressed by a point oblique type:

$$e - e_{c\max} = k_2\left(\lg p - \lg p_{c\max}\right), \tag{21}$$

where

$$k_2 = a_2 + 2a_3 \lg p_{c\max} + 3a_4\left(\lg p_{c\max}\right)^2. \tag{22}$$

The line IV equation is also represented by a point oblique type:

$$e - e_{c\max} = k\left(\lg p - \lg p_{c\max}\right), \tag{23}$$

where

$$k = -\tan\left[\frac{\arctan\left(-k_2\right)}{2}\right]. \tag{24}$$

Simultaneously solving equations (19) and (23) obtains the intersections $E(\lg p_c, e_c)$ of line I and line IV:

$$\lg p_c = \frac{e_{c\max} - k\lg p_{c\max} - \widehat{\beta}_0}{\widehat{k}_1 - k}. \tag{25}$$

3.4. Loess Damage Value of Sampling and Sample Preparation Disturbance. The saturated remolded loess compression curve is approximately straight:

$$e = A_s \lg p + B_s, \tag{26}$$

where A_s and B_s are the linear fitting coefficients of the saturated remolded loess.

Then, q_0 and q_r (equation (10)) change as follows:

$$q_0 = 10^{\lg p_c - \left(\lg p_c\right)_s} = 10^{\left(\left(e_{c\max} - k\lg p_{c\max} - \widehat{\beta}_0\right)/\left(\widehat{\mathbf{k}}_1 - k\right)\right) - \left(\left(e_c - B_s\right)/A_s\right)}, \tag{27}$$

$$\begin{aligned}
q_r &= 10^{\lg p_{c\max} - \left(\lg p_{c\max}\right)_s} \\
&= 10^{\left(\left(-B+(-1)^{n/2}m+(-1)^{n+1}\sqrt{S+(-1)^{n/2}T}\right)/4A\right) - \left(\left(e_{c\max} - B_s\right)/A_s\right)}.
\end{aligned} \tag{28}$$

Substituting equations (27) and (28) into equation (10) obtains the damage variable equation:

$$D = 1 - 10^{\left(\left(-B+(-1)^{n/2}m+(-1)^{n+1}\sqrt{S+(-1)^{n/2}T}\right)/4A\right) - \left(\left(e_{c\max} - B_s\right)/A_s\right) - \left(\left(e_{c\max} - k\lg p_{c\max} - \widehat{\beta}_0\right)/\left(\widehat{k}_1 - k\right)\right) + \left(\left(e_c - B_s\right)/A_s\right)}, \tag{29}$$

where q_r measured without the action of wetting and freeze-thaw cycles is q_{0r}. Additionally, substituting equations (27) and (28) into equation (10) obtains the sampling and sample preparation disturbance damage variable equation:

$$\left.\begin{array}{l}
D_d = 1 - 10^{\left(-B+(-1)^{n/2}m+(-1)^{n+1}\sqrt{S+(-1)^{n/2}T}/4A\right) - \left(\left(e_{c\max} - B_s\right)/A_s\right) - \left(\left(e_{c\max} - k\lg p_{c\max} - \widehat{\beta}_0\right)/\left(\widehat{k}_1 - k\right)\right) + \left(\left(e_c - B_s\right)/A_s\right)} \\
(\text{when } w = 2.5,\ n = 0 \text{ time})
\end{array}\right\}. \tag{30}$$

According to the test data, the compression curve of sampling and sample preparation disturbance of the loess can be fitted as follows:

$$e = 0.0349x^3 + 0.1359x^2 - 0.1385x + 0.9212, \quad r^2 = 0.956. \tag{31}$$

The regression line of the sampling and sample preparation disturbance of the loess at the end compression curve is as follows:

$$e = -0.2632x + 1.6512, \quad r^2 = 0.956. \tag{32}$$

The compression curve of saturated remolded loess can be fitted as follows:

$$e = -0.0002x + 0.8685, \quad r^2 = 0.967. \tag{33}$$

Based on the above deduction process, the calculation parameters need to be determined as follows (Table 3).

Substituting the calculation parameters into equation (30) obtains $D_d = 0.177$.

3.5. Structural Strength Damage of Loess under Wetting and Freeze-Thaw Cycles. Using the same method, the calculated parameters under different water contents and

Table 3: Calculation parameters.

Parameters	A	B	C	D	E	m	S	T	$P_{c\,\max}$	$e_{c\,\max}$	P_c	e_c
Value	$-4.34E-04$	$2.12E-03$	$-6.94E-03$	$2.95E-03$	$3.39E-02$	$1.88E-05$	$-3.54E-06$	$1.23E-05$	851.14	0.857	1035.18	0.834

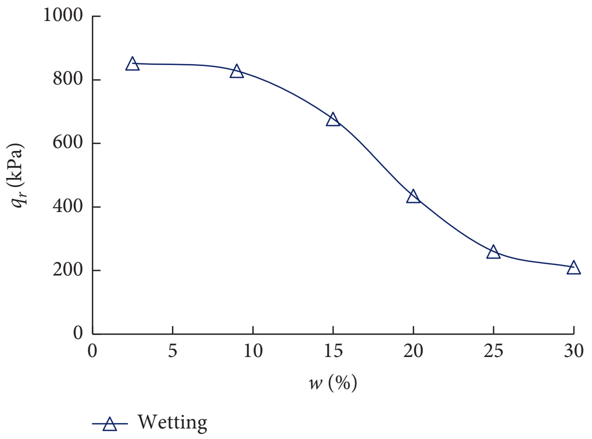

Figure 21: Residual structural strength of loess after wetting.

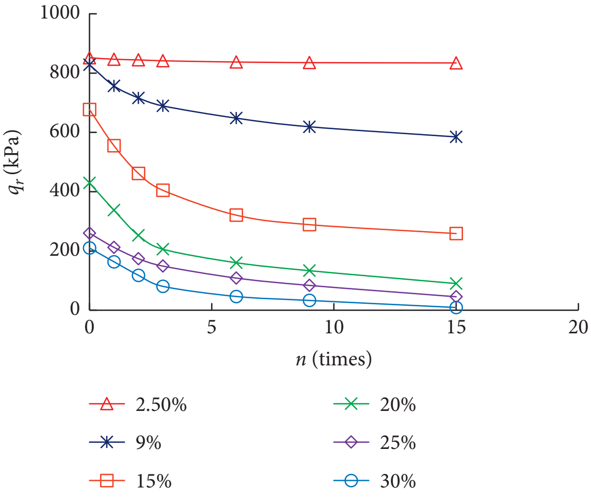

Figure 22: Residual structural strength of loess after freeze-thaw cycles.

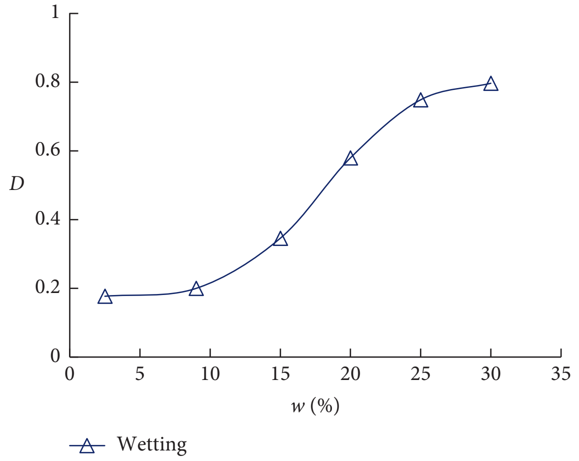

Figure 23: Deterioration law of the loess structural strength after wetting.

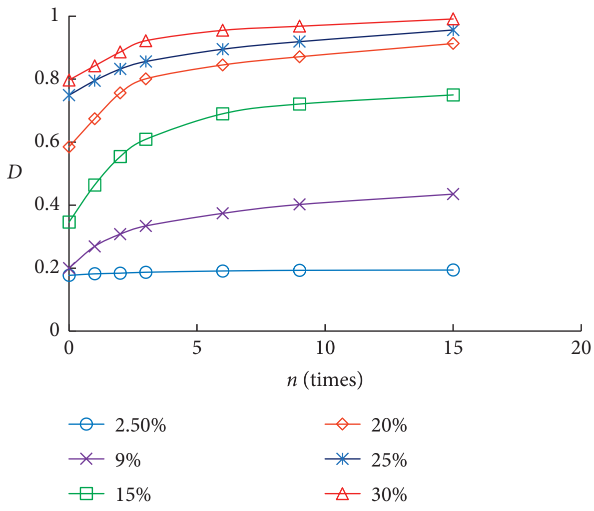

Figure 24: Deterioration law of the loess structural strength after freeze-thaw cycles.

freeze-thaw cycles can be obtained and substituted into equations (28) and (29) to obtain the residual structural strength and damage variables of the loess under wetting and freeze-thaw cycles. The changing rules are shown in Figures 21–24.

With an increase in water content, the loess residual structural strength (Figure 21) decreases according to the following pattern. When $w \leq w_p$, the decrease rate of q_r is slower, which indicates that the cementing structural strength and the friction structural strength are slightly reduced in the loess structure. When $w_P \leq w \leq w_L$, the decrease rate of q_r is faster, which indicates that cementing structural strength and friction structural strength are greatly reduced in the loess structure. When $w > w_L$, the decrease rate of q_r slows down, which indicates that the friction structural strength is basically reduced to zero, and the cementing structural strength reaches a limit in the loess structure.

The residual structural strength of the loess (Figure 22) will continue to decrease with an increase in the number of freeze-thaw cycles on the basis of moisture-related degradation, and the change trend is as follows. When the water content is very low, the residual structural strength does not change, or there is a slight decrease with the increase in the number of freeze-thaw cycles, which indicates that the cementing structural strength and friction structural strength do not change or change slightly. When $w_P \leq w \leq w_L$, the residual structure strength of the loess decreases the fastest before 6 freeze and thaw cycles, which indicates that the frozen-phase transformation causes the loess structure to produce many large pores, the cementing structural strength is reduced greatly, and the friction structural strength is reduced slightly. After 6 freeze and thaw cycles, the decrease rate of the loess residual structural strength becomes slower, which indicates that secondary structure is produced slowly. When $w > w_L$, the residual structure strength of loess also decreases faster before 6 freeze and thaw cycles, which indicates that the larger pore skeleton structure has been produced and increases in quantity. After 6 freeze and thaw cycles, the rate of decrease slows, which indicates that the secondary structure is basically formed.

Figures 23 and 24 show the following. (1) With an increase in water content, the damage variable of the loess increases, which shows that when $w < w_P$, the damage variable changes slowly; when $w_P < w < w_L$, the damage variable changes faster; and when $w > w_L$, the damage variable becomes slower again. (2) The degradation behavior of the loess structural strength during the freeze-thaw cycles with different water contents continues to increase based on wetting damage. (3) When the water content is low, the structural strength of the undisturbed loess is not affected or is only slightly affected by the freeze-thaw cycle. (4) Under different water content conditions, as the freeze-thaw cycles increase, the degree of deterioration of the loess structural strength increases first and then slows down. The concrete performance is as follows. When $w_P < w < w_L$, the intensity degradation curve of loess structure is steeper between 1 and 6 cycles. After 6 cycles, the curve becomes slower and the secondary substructure is slowly formed; when $w > w_P$, the structural deterioration curve of loess structure is somewhat steep between 1 and 6 cycles. After 6 cycles, the curve is basically gentle and the structure of the lower secondary structure is gradually formed.

4. Loess Structural Strength Deterioration Model

After the sampling and sample preparation processes are disturbed, the loess structural strength can be referred to as the loess residual structural strength after sampling and sample preparation disturbances and expressed as q_{0r}. After wetting, the loess structural strength can be called the wetting-damaged loess residual structural strength, expressed by q_{wr}. After freeze-thaw cycles, the loess structural strength can be referred to as frost heave-damaged loess residual structural strength and expressed as q_{nr}. The damage variables corresponding to the loess residual structural strength are as follows: the sampling and sample preparation disturbance damage variable, expressed as D_d; the wetting damage variable, expressed by D_w; and the frost heave damage variable, expressed by D_d. The damage variables are all microscopic statistical damage variables, so they do not affect each other. Therefore, the basic equations of damage to loess structural strength can be established as follows:

$$q_{0r} = q_0 \left(1 - D_d\right), \tag{34}$$

$$q_{wr} = q_0 \left(1 - D_d - D_w\right), \tag{35}$$

$$q_{nr} = q_0 \left(1 - D_d - D_w - D_n\right). \tag{36}$$

4.1. Loess Microscopic Statistical Damage Variable.

The loess microstructure is considered to be a comprehensive representation of loess microparticles or microparticle aggregates and their geometric arrangement and cementation. The loess microstructure has a certain structural strength, which is the ability of loess to maintain the original basic unit structure without being destroyed. Under external environmental disturbances and loads, the loess microstructure is weakened, and the soil skeleton particles are deformed and destroyed. The mechanical behavior of these microstructures shows that the macroscopic physical factors follow the Weibull distribution. In accordance with the Weibull distribution, the probability of the values of these random variables can be calculated and inferred, and the related problems of engineering technology can be solved.

Krajcinovic and Silva [54] proposed a statistical damage model based on the theory of continuous damage mechanics and strength statistics. Subsequently, the method was adopted by other scholars. In recent years, Wang et al. [55] and Li et al. [56] used the statistical method to describe rock evolution (initiation, growth, and coalescence) from damage to fracture with a continuous process and proposed a damage-softening statistical constitutive model for rock according to the Weibull distribution of mesoscopic element strength. Xie et al. [57] also established a loessial soil damage constitutive model based on the strength of loessial soil microunits with a Weibull distribution. Lai et al. [58] investigated the strength distribution patterns for warmed frozen clay and warmed ice-rich frozen clay based on the characteristics of the random distribution of defects in both clays. Jian and Gu [59] used the theory of continuous damage mechanics together with statistical mesoscopic strength theory based on a maximum entropy distribution to present a statistical damage constitutive model for rocks exhibiting strain softening behavior. Wen et al. [60] proposed the acoustic emission (AE) evolution model of rock failure according to the view that rock damage and AE were consistent. Zhang et al. [61] established a constitutive model for freeze-thaw damage to rock under three-dimensional stresses considering the random characteristics of the defects of rock materials. Zhu et al. [62] and Zhang et al. [63] also conducted in-depth research on the frozen soil damage model.

The loess microstructure is assumed to be composed of microunits such as different soil particles or particle clusters. The following statistical damage model was proposed by Krajcinovic and Silva [54]:

$$\sigma = E\varepsilon\left(1 - \frac{N_1}{N} - \frac{N_2}{N} - \frac{N_3}{N} - \cdots\right), \tag{37}$$

where E is the elastic modulus; ε is the strain; N_i is the number of microcells that fail under the action of the i^{th}; and N is the total number of microunits.

In this paper, the volume expansion ratio is taken as the test variable, and the probability density function $P(\eta)$ of the Weibull distribution can be expressed as follows:

$$P(\eta) = \frac{\beta}{F_0}\left(\frac{\eta}{F_0}\right)^{\beta-1} \text{esp}\left[-\left(\frac{\eta}{F_0}\right)^{\beta}\right], \quad \eta > 0, \tag{38}$$

where β is the shape parameter; F_0 is the scale parameter; and η is the volume expansion rate.

By analyzing equations (34)–(36) and equation (37) separately, the random damage variable can be defined as the ratio of N_i to N. The single-factor damage variables in this paper are D_d, D_w, and D_n. We further assume that when each volume expansion rate reaches a certain level η_d, η_{w}, and η_n, the number of damaged units is $N(\eta_d)$, $N(\eta_w)$, and $N(\eta_n)$, respectively.

$$D_d = \frac{N(\eta_d)}{N} = \frac{\int_0^{\eta_d} NP(x)\mathrm{d}x}{N}, \tag{39}$$

$$D_w = \frac{N(\eta_w)}{N} = \frac{\int_{\eta_d}^{\eta_w} NP(w)\mathrm{d}w}{N}, \tag{40}$$

$$D_n = \frac{N(\eta_n)}{N} = \frac{\int_{\eta_w}^{\eta_n} NP(n)\mathrm{d}n}{N}. \tag{41}$$

At a certain depth, the soil is in a state of stress balance. During the sampling process, the complex formation pressure of the loess is released, which causes a certain volume expansion. It is impossible to determine the volume change of the loess with a direct test, so the statistical damage model cannot be used to determine D_d. However, the D_d size has been obtained from the above experimental data fitting curve, i.e., $D_d = 0.177$.

According to Figure 19, the relationship between the volume of the preconsolidation pressure and the volume after the release of the sample pressure is as follows:

$$e_0 = e_c + (1 + e_c)\frac{\Delta V_d}{V_c} = e_c + (1 + e_c)\frac{\Delta V_d}{V - \Delta V_d}. \tag{42}$$

Figure 19 and Tables 1 and 3 show that $e_0 = 0.92$, $p_c = 1035.18$ kPa, and $e_c = 0.834$. Substituting these data into equation (42) yields $\Delta V_d = 5.375\,\mathrm{cm}^3$. Therefore, the sample of a ring knife can be reduced to the volume under the prior pressure as follows:

$$V_c = V - \Delta V_d = 120 - 5.375 = 114.625\,\mathrm{cm}^3. \tag{43}$$

Therefore, the sampling process disturbance expansion rate is as follows:

$$\begin{aligned} \eta_d' &= \frac{\Delta V_d}{V_c} \times 100\% = 4.69\%, \\ V_c &= \frac{V}{(1 + \eta_d')}. \end{aligned} \tag{44}$$

Similarly, the test expansion rate of the loess under the wetting and freeze-thaw cycles can be reduced to the prior pressure as follows:

$$\begin{aligned} \eta_w' &= \frac{\Delta V_w}{V_c} \times 100\% = \frac{\Delta V_w}{V}(1 + \eta_d') \times 100\% = \eta_w(1 + \eta_d'), \\ \eta_n' &= \frac{\Delta V_n}{V_c} \times 100\% = \frac{\Delta V_n}{V}(1 + \eta_d') \times 100\% = \eta_n(1 + \eta_d'), \\ \eta' &= \eta_d' + \eta_w' + \eta_n'. \end{aligned} \tag{45}$$

Substituting η_d', η_w', and η_n' into equations (39)–(41) provides the following equations:

$$D_d = \frac{N(\eta_d)}{N} = \frac{\int_0^{\eta_d} NP(x)\mathrm{d}x}{N}, \tag{46}$$

$$D_w = \frac{N(\eta_w)}{N} = \frac{\int_{\eta_d}^{\eta_w} NP(w)\mathrm{d}w}{N}, \tag{47}$$

$$D_n = \frac{N(\eta_n)}{N} = \frac{\int_{\eta_w}^{\eta_n} NP(n)\mathrm{d}n}{N}. \tag{48}$$

Next, substituting equation (38) into equations (46)–(48), D_d, D_w, and D_n can be obtained as follows:

$$\begin{aligned} D_d &= 1 - \exp\left[-\left(\frac{\eta_d'}{F_{d0}}\right)^{\beta_d}\right] = 0.177, \\ D_w &= \exp\left[-\left(\frac{\eta_d'}{F_{d0}}\right)^{\beta_d}\right] - \exp\left[-\left(\frac{\eta_w'}{F_{w0}}\right)^{\beta_w}\right], \\ D_n &= \exp\left[-\left(\frac{\eta_w'}{F_{w0}}\right)^{\beta_w}\right] - \exp\left[-\left(\frac{\eta_n'}{F_{n0}}\right)^{\beta_n}\right]. \end{aligned} \tag{49}$$

Based on the irreversible and superposition principles of damage mechanics, the damage variable of the strength of the undisturbed loess structure and the combined effects of wetting and freeze-thaw cycles can be defined as follows:

$$D = \begin{cases} D_d = 0.177, \\ D_w = 1 - \exp\left[-\left(\dfrac{\eta_w'}{F_{w0}}\right)^{\beta_w}\right], \\ D_n = 1 - \exp\left[-\left(\dfrac{\eta_n'}{F_{n0}}\right)^{\beta_n}\right]. \end{cases} \tag{50}$$

4.2. Microscopic Statistical Damage Model of Loess.

In this paper, the volume expansion ratio is taken as the test variable. Figure 25 shows that the volume expansion ratio of the loess increases with the water content. Initially, the growth is slow, and then the growth is accelerated. To improve the accuracy, the two straight lines are shown in Table 4.

The function of the relationship between the volume expansion ratio and the water content of loess is $\eta_w' = f(w)$ and divided into two straight lines, that is,

$$f(w) = \begin{cases} a_1 w + b_1, & \text{if } w \le w_p, \\ a_2 w + b_2, & \text{if } w > w_p, \end{cases} \tag{51}$$

where a_1, a_2, b_1, and b_2 are fitting factors for the experiment and can be calculated from the test data, where $a_1 < a_2$.

Figure 26 shows that the undisturbed loess sample (water content is 2.5%) does not change the volume of the loess with an increase in the number of freeze-thaw cycles, which indicates that the freeze-thaw cycle does no damage to the structural strength of the loess. At other water contents, the

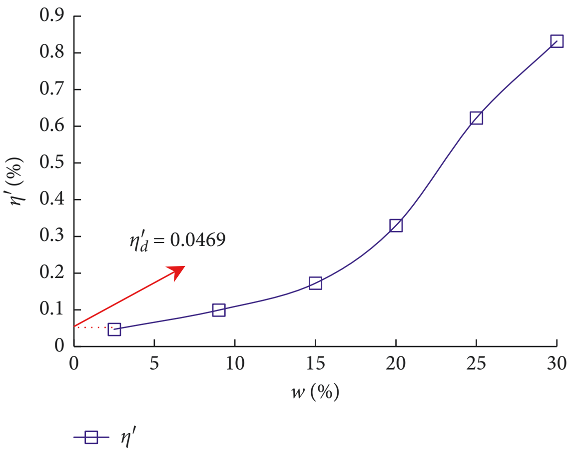

Figure 25: Volume change after wetting.

Table 4: Fitting formula for loess expansion rate under wetting.

w (%)	Fitting function	R^2
$w \le w_P$	$\eta_w' = 0.01w - 0.0177$	0.9859
$w > w_P$	$\eta_w' = 0.05w - 0.6615$	0.9908

number of freeze-thaw cycles increases the volume expansion ratio of loess in the first period, the growth is faster, and then the growth slows down. To improve the accuracy, the two straight lines are shown in Table 5.

The function of the relationship between the volume expansion ratio of loess and the freeze-thaw cycles in cases of different water contents is $\eta_n' = f(w, n)$ and is divided into two straight lines, that is,

$$f(w, n) = \begin{cases} c_1 n + d_1, & \text{if} n \le 3, \\ c_2 n + d_2, & \text{if} n > 3, \end{cases} \tag{52}$$

where c_1, c_2, d_1, and d_2 are the test fitting coefficients, which can be calculated from the test data, and $c_1 > c_2$.

Substituting the functions $f(w)$ and $f(w, n)$ into equations (38) and (50) yields a damage probability density function for wetting and freeze-thaw cycles and a damage variable for wetting and freeze-thaw cycles.

The damage probability density function in the process of wetting is expressed as follows:

$$P(w) = \frac{\beta_w}{F_{w0}} \left(\frac{a_i w + b_i}{F_{w0}} \right)^{\beta_w - 1} \exp\left[-\left(\frac{a_i w + b_i}{F_{w0}} \right)^{\beta_w} \right], \tag{53}$$

where $i = 1$ or 2, as determined by equation (51).

The damage probability density function with increasing number of freeze-thaw cycles in different water contents is expressed as follows:

$$P(w, n) = \frac{\beta_n}{F_{n0}} \left(\frac{c_i n + d_i}{F_{n0}} \right)^{\beta_n - 1} \exp\left[-\left(\frac{c_i n + d_i}{F_{n0}} \right)^{\beta_n} \right], \tag{54}$$

where $i = 1$ or 2, which is determined by equation (52).

The damage variable for the wetting and freeze-thaw cycles is expressed as follows:

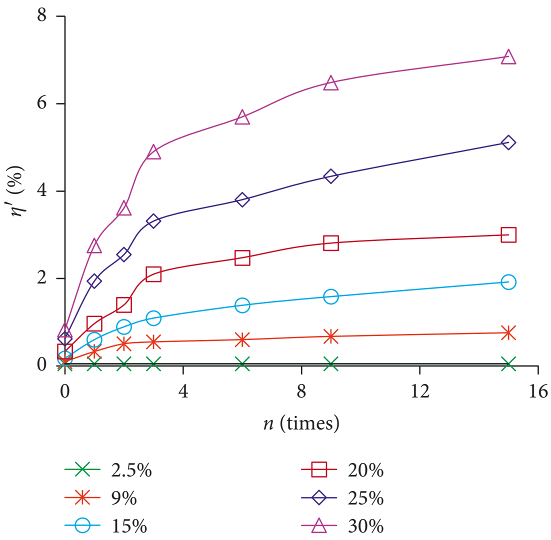

Figure 26: Volume change after freeze-thaw cycles.

Table 5: Fitting formula for loess expansion rate under freeze-thaw cycles.

w (%)	n	Fitting function	R^2
9	$n \le 3$	$\eta_n' = 0.1528n + 0.1422$	0.9268
	$n > 3$	$\eta_n' = 0.0169n + 0.509$	0.9772
15	$n \le 3$	$\eta_n' = 0.3057n + 0.2322$	0.9722
	$n > 3$	$\eta_n' = 0.0588n + 1.043$	0.9981
20	$n \le 3$	$\eta_n' = 0.5737n + 0.3379$	0.9924
	$n > 3$	$\eta_n' = 0.0543n + 2.2185$	0.8822
25	$n \le 3$	$\eta_n' = 0.8679n + 0.8049$	0.9704
	$n > 3$	$\eta_n' = 0.1431n + 2.9887$	0.9929
30	$n \le 3$	$\eta_n' = 1.3076n + 1.0666$	0.9756
	$n > 3$	$\eta_n' = 0.1458n + 4.9643$	0.9295

$$D = \begin{cases} D_d = 0.177, \\ D_w = 1 - \exp\left[-\left(\dfrac{a_i w + b_i}{F_{w0}} \right)^{\beta_w} \right], \\ D_n = 1 - \exp\left[-\left(\dfrac{c_i n + d_i}{F_{n0}} \right)^{\beta_n} \right]. \end{cases} \tag{55}$$

The first derivative of equation (54) can be used to obtain the wetting damage evolution function $g(w)$ and the freeze-thaw cycle damage evolution function $g(w, n)$:

$$\begin{aligned} g(w) &= \frac{\mathrm{d}D}{\mathrm{d}w} = a_i \frac{\beta_w}{F_{w0}} \left(\frac{a_i w + b_i}{F_{w0}} \right)^{\beta_w - 1} \exp\left[-\left(\frac{a_i w + b_i}{F_{w0}} \right)^{\beta_w} \right], \\ g(w, n) &= \frac{\partial D}{\partial n} = c_i \frac{\beta_n}{F_{n0}} \left(\frac{c_i n + d_i}{F_{n0}} \right)^{\beta_n - 1} \exp\left[-\left(\frac{c_i n + d_i}{F_{n0}} \right)^{\beta_n} \right]. \end{aligned} \tag{56}$$

Substituting equation (55) into equations (34)–(36), the basic model of statistical damage of loess structure strength wetting and freeze-thaw cycles is obtained:

$$q_{0r} = 0.823q_0, \tag{57}$$

$$q_{wr} = q_0\left\{\exp\left[-\left(\frac{a_i w + b_i}{F_{w0}}\right)^{\beta_w}\right] - 0.177\right\}, \tag{58}$$

$$q_{nr} = q_0\left\{\exp\left[-\left(\frac{a_i w + b_i}{F_{w0}}\right)^{\beta_w}\right] + \exp\left[-\left(\frac{c_i n + d_i}{F_{n0}}\right)^{\beta_n}\right] - 1.177\right\}. \tag{59}$$

4.3. Damage Model Parameter Determination. After a simple transformation of equations (58) and (59), the logarithm of the two sides of the equation can be obtained as follows:

$$-\ln\left(\frac{q_{wr}}{q_0} + 0.177\right) = \left(\frac{a_i w + b_i}{F_{w0}}\right)^{\beta_w}, \tag{60}$$

$$-\ln\left(\frac{q_{nr}}{q_0} + 1.177\right) = \left(\frac{a_i w + b_i}{F_{w0}}\right)^{\beta_w} + \left(\frac{c_i n + d_i}{F_{n0}}\right)^{\beta_n}. \tag{61}$$

The model parameters β_w, β_n, F_{w0}, and F_{n0} can be calculated by substituting the test fitting coefficients in Tables 4 and 5 into equations (60) and (61), respectively.

By substituting the model parameters of Table 6 into equation (55), the model of water-absorbing wetting and hydration damage to the loess structure can be obtained.

$$D_w = \begin{cases} 1 - \exp\left[-\left(\dfrac{0.0096w - 0.0279}{0.2158}\right)^{2.7209}\right], & \text{if } w \le w_p, \\ 1 - \exp\left[-\left(\dfrac{0.048w - 0.6767}{0.804}\right)^{0.6346}\right], & \text{if } w > w_p. \end{cases} \tag{62}$$

By substituting the model parameters of Table 6 into equation (55), the damage model coupling strength, wetting and freeze-thaw cycles of the loess structure can be obtained.

When $w \le w_P$,

$$D_{w,n} = \begin{cases} 1 - \exp\left[-\left(\dfrac{c_1 n + d_1}{4.4602}\right)^{0.7566}\right], & \text{if } n \le 3, \\ 1 - \exp\left[-\left(\dfrac{c_2 n + d_2}{1.2713}\right)^{1.5869}\right], & \text{if } n > 3. \end{cases} \tag{63a}$$

When $w > w_P$,

$$D_{w,n} = \begin{cases} 1 - \exp\left[-\left(\dfrac{c_1 n + d_1}{0.57}\right)^{0.1638}\right], & \text{if } n \le 3, \\ 1 - \exp\left[-\left(\dfrac{c_2 n + d_2}{0.5308}\right)^{0.256}\right], & \text{if } n > 3. \end{cases} \tag{63b}$$

TABLE 6: Model parameters.

	Subsection condition		β_w	F_{w0}
Wetting	$w \le w_P$		2.7209	0.2158
	$w > w_P$		0.6346	0.804
	Subsection condition		β_n	F_{n0}
Freeze-thaw cycles	$w \le w_P$	$n \le 3$	0.7566	4.4602
		$n > 3$	1.5869	1.2713
	$w > w_P$	$n \le 3$	0.1638	0.57
		$n > 3$	0.256	0.5308

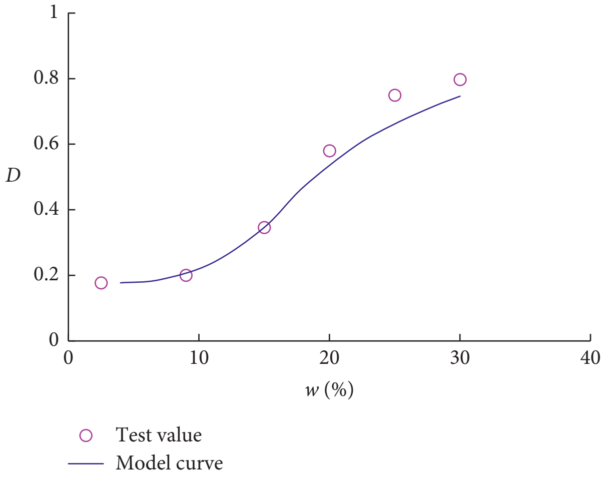

FIGURE 27: Validation of the loess wetting damage model.

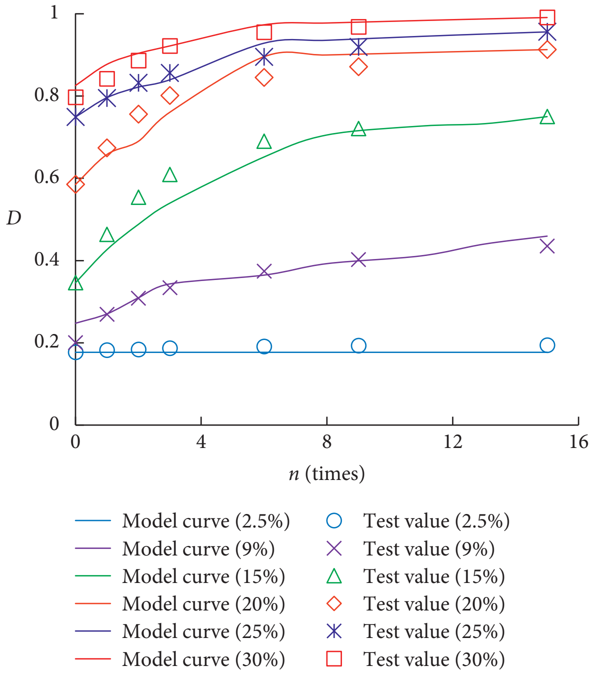

FIGURE 28: Validation of the loess wetting and freeze-thaw cycle damage model.

4.4. Model Verification. Under the coupling of different water contents and freeze-thaw cycles, through a side compression test of Q_3 loess taken from a foundation pit in the northern suburbs of Xi'an, the damage degradation value was obtained by using the calculation method described in this paper, and the damage model was verified.

As shown in equation (62) and Figure 27, when $w < w_P$, the water absorption and wetting hydration model curve predicts the damage value to be consistent with the experimental value. When $w > w_P$, the model predicts the damage value to be lower than the experimental value. Therefore, the model needs to be revised for specific projects.

Equations (63a) and (63b) and Figure 28 are used to produce the wetting and freeze-thaw cycles coupling model curve. To improve the accuracy of the model, the segmentation conditions are refined according to the water content and the number of freeze-thaw cycles. When $w < w_P$, the predicted damage value of the model is basically consistent with the experimental value with the increase in the number of freeze-thaw cycles. The predicted damage value of the model is lower than the experimental value at individual water contents. When $w > w_P$, when the number of freeze-thaw cycles is $n < 3$, the model predicts the damage value. Compared with the experimental values, when the number of freeze-thaw cycles $n > 3$, the predicted damage value of the model is higher than the experimental value; thus, the engineering design is conservative and safe.

From Equations (62), (63a), and (63b), the basic model of damage to the loess structure through the water-soil interaction and the coupling of wetting and freeze-thaw cycles can be applied to collapsible loess, which decreases in volume during wetting. During the subsequent process, the volume increases, the wetting volume decreases again, and the refreeze volume increases. Such repeated changes need to be corrected and discussed in equations (51) and (52), which is beyond the scope of this article.

5. Conclusions

(1) Laboratory experiments were conducted to study the volume and pore structure of loess samples with the changes caused by wetting and freeze-thaw cycles, and the change trends for the expansion ratio and void ratio were obtained. Second, microscopic testing technology (SEM) and digital image analysis technology (IPP 6.0) were used to investigate the variations in the microscopic particle size and pore ratio of loess with the number of freeze-thaw cycles at $w = 20\%$. The results are very close to those of the geotechnical test. This method represents a new approach for the analysis of the microscopic pore structure of loess. Finally, the variations in the compressive index C_c and compressive modulus E_s of loess with wetting and freeze-thaw cycles were investigated according to the confined compression test.

(2) According to the e-lg$p$ compression curve, the principle of yield failure of loess structure was analyzed, and the loess structural strength, residual structural strength, and damage variable were newly defined. Additionally, combined with confined compression test data and mathematical statistics, the damage value generated by the disturbances during the sampling and preparation of loess was determined, and the deterioration of the structural strength and damage variable of loess was analyzed.

(3) Based on microscopic statistical damage theory and the Weibull distribution, statistical damage variables considering the disturbances in sampling, sample preparation processes, wetting and freeze-thaw cycles were established. Then, the volume expansion ratio of loess was used as the variable for the Weibull distribution. According to the experimental data, the expansion rate function under wetting and freeze-thaw cycles was fitted, and the statistical damage model parameters and the damage models of wetting and freeze-thaw cycles were solved by using the coefficient of expansion function and the basic equation of damage. Finally, the damage model was verified using data of loess taken from a foundation pit in the northern suburbs of Xi'an. The model-predicted damage value was consistent with the experimental value. The statistical damage model has good practicability and can for provide guidance for practical engineering design and construction.

Data Availability

The data used to support the findings of this study are included within the article.

Conflicts of Interest

The authors declare no conflicts of interest.

Acknowledgments

This work was supported by the National Natural Science Foundation of China (nos. 51674200, 51874320, 51604285, and 51868075), the Science and Technology Innovation Project of Key Laboratory of Shaanxi Province China (no. 2014SZS15–Z02), the Yan'an University Doctor Scientific Research Initialization Foundation (no. YDBK2018-52), and the Open Foundation of Key Laboratory of Failure Mechanism and Safety Control Techniques of Earth-Rock Dam of the Ministry of Water Resources (YK916006), which are gratefully acknowledged.

References

[1] C. D. F. Rogers, T. A. Dijkstra, and I. J. Smalley, "Hydroconsolidation and subsidence of loess: studies from China, Russia, North America and Europe," *Engineering Geology*, vol. 37, no. 2, pp. 83–113, 1994.

[2] S. C. Porter, "Loess records | China," in *Encyclopedia of Quaternary Science*, A. E. Scott, Ed., pp. 1429–1440, Elsevier, Oxford, UK, 2007, http://www.sciencedirect.com/science/article/B8F8W-4MWJ3HV-57/2/d6216edcc660898fe02293509996630d.

[3] T. T. Kie, “Fundamental properties of loess from Northwestern China,” *Engineering Geology*, vol. 25, no. 2–4, pp. 103–122, 1988.

[4] J. Sun, “Source regions and formation of the loess sediments on the high mountain regions of northwestern China,” *Quaternary Research*, vol. 58, no. 3, pp. 341–351, 2002.

[5] E. Derbyshire and T. W. Mellors, “Geological and geotechnical characteristics of some loess and loessic soils from China and Britain: a comparison,” *Engineering Geology*, vol. 25, no. 2–4, pp. 135–175, 1988.

[6] M. Jiang, F. Zhang, H. Hu, Y. Cui, and J. Peng, “Structural characterization of natural loess and remolded loess under triaxial tests,” *Engineering Geology*, vol. 181, pp. 249–260, 2014.

[7] Z. Lei, Y. Huang, P. Sun, F. Yang, and Q. Zhang, “Analysis on the characteristics of loess collapsibility in loess plateau, Northern Shaanxi province,” in *Proceedings of the International Symposium on Water Resource & Environmental Protection*, pp. 2704–2707, Xi’an, China, May 2011.

[8] C. J. Van Westen, T. W. J. Van Asch, and R. Soeters, “Landslide hazard and risk zonation-why is it still so difficult?,” *Bulletin of Engineering Geology and the Environment*, vol. 65, no. 2, pp. 167–184, 2006.

[9] J. S. Shi, L. Z. Wu, S. R. Wu, B. Li, T. Wang, and P. Xin, “Analysis of the causes of large-scale loess landslides in Baoji, China,” *Geomorphology*, vol. 264, pp. 109–117, 2016.

[10] H. Qiu, Y. Cui, S. Hu, D. Yang, Y. Pei, and W. Yang, “Temporal and spatial distributions of landslides in the Qinba mountains, Shaanxi province, China,” *Geomatics, Natural Hazards and Risk*, vol. 10, no. 1, pp. 599–621, 2019.

[11] F. Yang and G. Wang, “Effect of irrigation-induced densification on the post-failure behavior of loess flowslides occurring on the Heifangtai area, Gansu, China,” *Engineering Geology*, vol. 236, no. 11, pp. 111–118, 2018.

[12] X. Shao, H. Zhang, and Y. Tan, “Collapse behavior and microstructural alteration of remolded loess under graded wetting tests,” *Engineering Geology*, vol. 233, pp. 11–22, 2018.

[13] B. Dušan, B. Zoran, V. Čebašek, and N. Šušić, “Characterisation of collapsing loess by seismic dilatometer,” *Engineering Geology*, vol. 181, pp. 180–189, 2014.

[14] T. Miao and Z. Wang, “The deformation mechanism of collapsible loess based on instability of microstructure,” *Science China (Series B)*, vol. 20, no. 1, pp. 86–96, 1990.

[15] A. I. Calderhead, A. Martel, P.-J. Alasset, A. Rivera, and J. Garfias, “Land subsidence induced by groundwater pumping, monitored by D-INSAR and field data in the Toluca Valley, Mexico,” *Canadian Journal of Remote Sensing*, vol. 36, no. 1, pp. 9–23, 2010.

[16] S. Figueroa-Miranda, J. Tuxpan-Vargas, J. Alfredo Ramos-Leal, V. M. Hernández-Madrigal, and C. I. Villaseñor-Reyes, “Land subsidence by groundwater over-exploitation from aquifers in tectonic valleys of Central Mexico: a review,” *Engineering Geology*, vol. 246, pp. 91–106, 2018.

[17] S. Xu and T. Zhao, “The loess slope stability study,” *Applied Mechanics & Materials*, vol. 380–384, pp. 4827–4829, 2013.

[18] F. C. Dai, C. F. Lee, and Y. Y. Ngai, “Landslide risk assessment and management: an overview,” *Engineering Geology*, vol. 64, no. 1, pp. 65–87, 2002.

[19] C. H. Zhou, C. F. Lee, Li ., and Z. W. J. Li, “On the spatial relationship between landslides and causative factors on Lantau Island, Hong Kong,” *Geomorphology*, vol. 43, no. 3-4, pp. 197–207, 2002.

[20] R. Huang, “Some catastrophic landslides since the twentieth century in the southwest of China,” *Landslides*, vol. 6, no. 1, pp. 69–81, 2009.

[21] W. Gong, C. H. Juang, and J. R. Martin, “A new framework for probabilistic analysis of the performance of a supported excavation in clay considering spatial variability,” *Géotechnique*, vol. 67, no. 6, pp. 546–552, 2017.

[22] K. Terzaghi, *Theoretical Soil Mechanics*, Wiley and Sons, New York, USA, 1943.

[23] K. Collins and A. Mcgown, “The form and function of microfabric features in a variety of natural soils,” *Géotechnique*, vol. 24, no. 2, pp. 223–254, 1974.

[24] A. Casagrande, “The structure of clay and its importance in foundation engineering,” *Boston Society Civil Engineers Journal*, vol. 19, no. 4, pp. 168–209, 1932.

[25] K. Soga, *Mechanical Behavior and Constitutive Modeling of Natural Structured Soils*, Department of Civil and Environmental Engineering, University of California, Berkeley, CA, USA, 1994.

[26] D. Lafeber, “Soil structural concepts,” *Engineering Geology*, vol. 1, no. 4, pp. 261–290, 1966.

[27] R. A. Lohnes and T. Demirel, “Strength and structure of laterites and lateritic soils,” *Engineering Geology*, vol. 7, no. 1, pp. 13–33, 1973.

[28] G. Gao, “Classification of collapsibility structure and collapsibility of loess,” *Science in China (Series C)*, vol. 23, no. 12, pp. 1–9, 1980.

[29] Z. Shen, “Soil structural mathematical model: the core issue of soil mechanics in the 21st century,” *Chinese Journal of Geotechnical Engineering*, vol. 18, no. 1, pp. 95–97, 1996, in Chinese.

[30] D. Xie and J. Qi, “Soil structure characteristics and new approach in research on its quantitative parameter,” *Chinese Journal of Geotechnical Engineering*, vol. 21, no. 6, pp. 651–656, 1999, in Chinese.

[31] Y. Luo, D. Xie, and S. Shao, “Structural parameter of soil under complex stress conditions,” *Chinese Journal of Rock Mechanics and Engineering*, vol. 23, no. 24, pp. 4248–4251, 2004, in Chinese.

[32] Z. Chen, X. Fang, Y. Zhu, B. Qin, X. Wei, and Z. Yao, “Research on meso-structures and their evolution laws of expansive soil and loess,” *Rock and Soil Mechanics*, vol. 30, no. 1, pp. 1–11, 2009, in Chinese.

[33] Y. M. Reznik, “A method for calculation of soil structural pressure values,” *Engineering Geology*, vol. 78, no. 1-2, pp. 95–104, 2005.

[34] E.-L. Liu, H.-S. Yu, C. Zhou, Q. Nie, and K.-T. Luo, “A binary-medium constitutive model for artificially structured soils based on the disturbed state concept and homogenization theory,” *International Journal of Geomechanics*, vol. 17, no. 7, Article ID 04016154, 2017.

[35] O. Ahad, “Disturbed state concept-based constitutive model for structured soils,” *International Journal of Geomechanics*, vol. 17, no. 7, Article ID 04017008, 2017.

[36] C. Xu, X. Wang, X. Lu, F. Dai, S. Jiao, and Y. Gao, “Experimental study of residual strength and the index of shear strength characteristics of clay soil,” *Engineering Geology*, vol. 233, no. 3, pp. 183–190, 2018.

[37] E. J. Chamberlain and A. J. Gow, “Effect of freezing and thawing on the permeability and structure of soils,” *Engineering Geology*, vol. 13, no. 1–4, pp. 73–92, 1979.

[38] J. Qi, W. Ma, and C. Song, “Influence of freeze-thaw on engineering properties of a silty soil,” *Cold Regions Science and Technology*, vol. 53, no. 3, pp. 397–404, 2008.

[39] T. C. Johnson, D. M. Cole, and E. J. Chamberlain, “Effect of freeze-thaw cycles on resilient properties of fine-grained

soils," *Developments in Geotechnical Engineering*, vol. 13, no. 1, pp. 247–276, 1979.

[40] Y. Lu, S. Liu, L. Weng, L. Wang, Z. Wang, and L. Xu, "Fractal analysis of cracking in a clayey soil under freeze-thaw cycles," *Engineering Geology*, vol. 208, pp. 93–99, 2016.

[41] Z. Zhou, W. Ma, S. Zhang, Y. Mu, and G. Li, "Effect of freeze-thaw cycles in mechanical behaviors of frozen loess," *Cold Regions Science and Technology*, vol. 146, pp. 9–18, 2018.

[42] J. Xu, J. Ren, Z. Wang, S. Wang, and J. Yuan, "Strength behaviors and meso-structural characters of loess after freeze-thaw," *Cold Regions Science and Technology*, vol. 148, pp. 104–120, 2018.

[43] J. Xu, Y. Li, W. Lan, and S. Wang, "Shear strength and damage mechanism of saline intact loess after freeze-thaw cycling," *Cold Regions Science and Technology*, vol. 164, p. 102779, 2019.

[44] J. Dang and J. Li, "The structural strength and shear strength of unsaturated loess," *Journal of Hydraulic Engineering*, vol. 32, no. 7, pp. 79–83, 2001, in Chinese.

[45] Z. Hu, Z. Shen, and D. Xie, "Research on structural behavior of unsaturated loess," *Chinese Journal of Rock Mechanics and Engineering*, vol. 19, no. 6, p. 775, 2000, in Chinese.

[46] K. Tian, J. Ma, and Y. Li, "Discussion on quantitative parameters of loess structure," *Chinese Journal of Rock Mechanics and Engineering*, vol. 30, no. 1, pp. 3179–3184, 2011, in Chinese.

[47] K. Tian, P. Wang, and H. Zhang, "Discussion on stress-strain relation of intact loess considering soil structure," *Rock and Soil Mechanics*, vol. 34, no. 7, pp. 1893–1898, 2013, in Chinese.

[48] X. Yin, E. Liu, B. Song, and D. Zhang, "Numerical analysis of coupled liquid water, vapor, stress and heat transport in unsaturated freezing soil," *Cold Regions Science and Technology*, vol. 155, pp. 20–28, 2018.

[49] Y. Lu, S. Liu, E. Alonso, L. Wang, L. Xu, and Z. Li, "Volume changes and mechanical degradation of a compacted expansive soil under freeze-thaw cycles," *Cold Regions Science and Technology*, vol. 157, pp. 206–214, 2019.

[50] L. Tang, S. Cong, X. Ling, W. Xing, and Z. Nie, "A unified formulation of stress-strain relations considering micro-damage for expansive soils exposed to freeze-thaw cycles," *Cold Regions Science and Technology*, vol. 153, pp. 164–171, 2018.

[51] Y. Liu, R. Huang, E. Liu, and F. Hou, "Mechanical behaviour and constitutive model of tailing soils subjected to freeze-thaw cycles," *European Journal of Environmental and Civil Engineering*, vol. 22, pp. 1–23, 2018.

[52] E. Hou, Y. Lai, H. Wong, and J. Feng, "An elastoplastic model for saturated freezing soils based on thermo-poromechanics," *International Journal of Plasticity*, vol. 107, pp. 246–285, 2018.

[53] H. Zhang, C. Yuan, G. Yang et al., "A novel constitutive modelling approach measured under simulated freeze–thaw cycles for the rock failure," *Engineering with Computers*, vol. 35, no. 3, pp. 1–14, 2019.

[54] D. Krajcinovic and M. A. G. Silva, "Statistical aspects of the continuous damage theory," *International Journal of Solids and Structures*, vol. 18, no. 7, pp. 551–562, 1982.

[55] Z.-l. Wang, Y.-c. Li, and J. G. Wang, "A damage-softening statistical constitutive model considering rock residual strength," *Computers & Geosciences*, vol. 33, no. 1, pp. 1–9, 2007.

[56] X. Li, W.-G. Cao, and Y.-H. Su, "A statistical damage constitutive model for softening behavior of rocks," *Engineering Geology*, vol. 143-144, pp. 1–17, 2012.

[57] X. Xie, D. H. Wang, and F. S. Zhao, "Statistic damage constitutive model of loessial soil considering damage threshold," *Applied Mechanics and Materials*, vol. 204-208, pp. 370–375, 2012.

[58] Y. Lai, S. Li, J. Qi, Z. Gao, and X. Chang, "Strength distributions of warm frozen clay and its stochastic damage constitutive model," *Cold Regions Science and Technology*, vol. 53, no. 2, pp. 200–215, 2008.

[59] D. Jian and D. Gu, "On a statistical damage constitutive model for rock materials," *Computers & Geosciences*, vol. 37, no. 2, pp. 122–128, 2011.

[60] G.-c. Wen, H.-m. Yang, and Y.-h. Zou, "Theoretical analysis of characteristics of acoustic emission in rock failure based on statistical damage mechanics," *Journal of Coal Science and Engineering (China)*, vol. 15, no. 3, pp. 237–242, 2009.

[61] H. Zhang, X. Xie, C. Peng, G. Yang, W. Ye, and Y. Sheng, "Constitutive model for damage of freeze-thaw rock under three-dimensional stress," *Chinese Journal of Geotechnical Engineering*, vol. 39, no. 8, pp. 1444–1452, 2017, in Chinese.

[62] Z. Zhu, J. Ning, and W. Ma, "A constitutive model of frozen soil with damage and numerical simulation for the coupled problem," *Science China Physics, Mechanics and Astronomy*, vol. 53, no. 4, pp. 699–711, 2010.

[63] D. Zhang, E. Lui, X. Liu, and B. Song, "Investigation on binary medium model taking frozen silt soils under -6°C for example," *Chinese Journal of Geotechnical Engineering. Eng.*vol. 40, no. 1, pp. 82–90, 2018, in Chinese.

[64] S. Hu, X. Wang, and Y. Zhang, "The effects of slope length and slope gradient on the size distributions of loess slides: field observations and simulations," *Geomorphology*, vol. 300, pp. 69–76, 2018.


Advances in
Operations Research

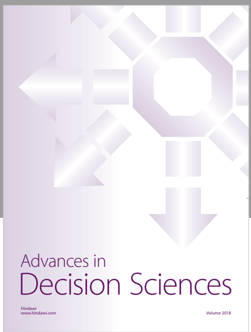
Advances in
Decision Sciences

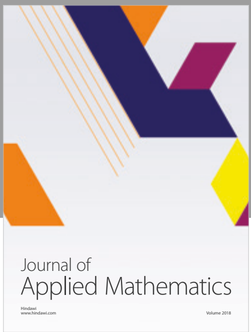
Journal of
Applied Mathematics


The Scientific
World Journal

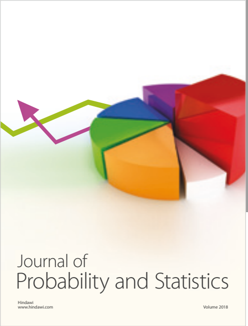
Journal of
Probability and Statistics

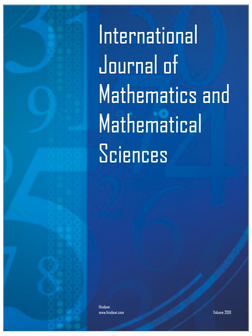
International
Journal of
Mathematics and
Mathematical
Sciences


Journal of
Optimization

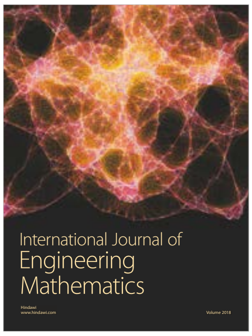
International Journal of
Engineering
Mathematics


International Journal of
Analysis

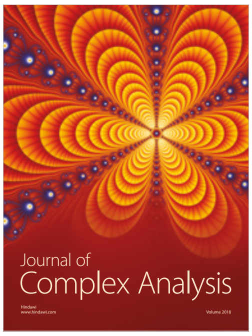
Journal of
Complex Analysis

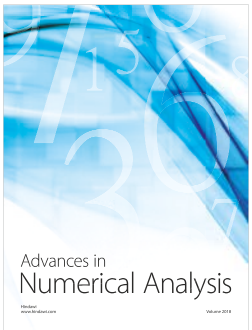
Advances in
Numerical Analysis

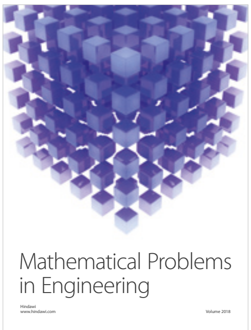
Mathematical Problems
in Engineering

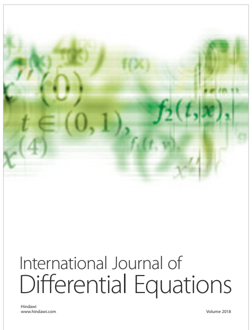
International Journal of
Differential Equations

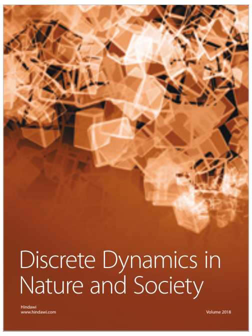
Discrete Dynamics in
Nature and Society

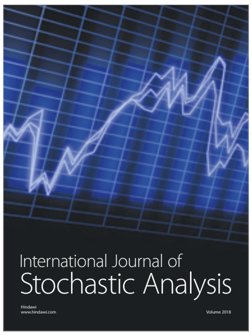
International Journal of
Stochastic Analysis


Journal of
Mathematics


Journal of
Function Spaces

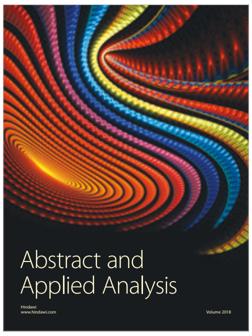
Abstract and
Applied Analysis

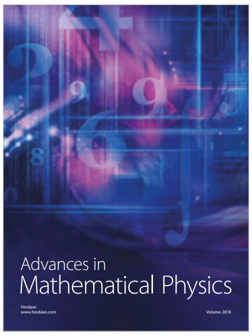
Advances in
Mathematical Physics